A COMPREHENSIVE STUDY OF STEADY AND TRANSIENT HEAT TRANSFER DURING SEMI-CONFINED LIQUID JET IMPINGEMENT WITH ROTATION

Muhammad M. RAHMAN and Jorge C. LALLAVE
Department of Mechanical Engineering
University of South Florida, Tampa, Florida 33620, USA
e-mail: rahman@eng.usf.edu

ABSTRACT

Steady and transient conjugate heat transfer from a uniformly heated spinning solid disk of finite thickness and radius during a semi–confined liquid jet impingement is studied for various disk materials, namely aluminum, copper, silver, Constantan, and silicon, covering a range of Reynolds number (220 – 900), Ekman number ($7.08x10^{-5}$ – ∞), disk thicknesses to nozzle diameter ratio ($b/d_n = 0.25 – 1.67$), confinement ratio ($r_p/r_d = 0.2 – 0.75$), and Prandtl number (1.29 – 124.44) using ammonia (NH_3), water (H_2O), flouroinert (FC–77) and oil (MIL–7808) as working fluids. Increasing the Reynolds number (Re_j) decreases the time to achieve the steady–state condition with its surroundings and increases the local and average Nusselt number. A higher rotational rate also increases the Nusselt number under most conditions. A higher thermal conductivity disk material maintains a lower temperature non–uniformity at the interface. The increment of confinement ratio (r_p/r_d) increases the interface temperature as it slows down the fluid momentum and the convective heat transfer rate. Increasing the disk thickness decreases the interface temperature and increases the duration of the transient.

KEYWORDS: *Semi–confined liquid jet impingement, Rotating disk, Free surface flow, Transient conjugate heat transfer.*

1. INTRODUCTION

The interaction of liquid jet impingement and rotation creates a complex and powerful flow capable of improving heat or mass transfer processes considerably. The high transport rate, along with the simplicity of hardware requirements makes this process an attractive option in applications such as metal etching, rinsing operations to dissolve species, surface coating, and microgravity fluid handling. A theoretical study of circular laminar impinging free jet spreading into a thin film was done by Watson [1]. A review of both analytical and experimental studies on jet impinging on a flat surface has been presented by Polat et al. [2]. Carper and Deffenbaugh [3] and Carper et al. [4] conducted experiments to determine the average heat transfer coefficient at the rotating disk, with uniform temperature cooled by a single liquid jet of oil impinging normal to the surface. Metzger et al. [5] employed liquid crystal for mapping the local heat transfer distribution on a rotating disk with jet impingement. Thomas et al. [6] measured the film thickness across a stationary and rotating horizontal disk using the capacitance technique, where the liquid was delivered to the disk by a controlled semi-confined impinging jet. Hung and Shieh [7] reported experimental measurements of heat transfer characteristics of jet impingement onto a horizontally rotating ceramic–based multichip disk. Ozar et al. [8] measured the thickness of the liquid film on the

disk surface by an optical method, including the characterization of the hydraulic jump. Rice et al. [9] presented an analysis of the liquid film and heat transfer characteristics of a free surface controlled liquid jet impingement onto a rotating disk.

Transient heat transfer during jet impingement has been the subject matter in only a few past studies. Fujimoto et al. [10] presented a numerical simulation of transient cooling of a hot solid by an impinging circular free surface liquid jet. The flow and thermal fields in the liquid as well as the temperature distributions in the hot solid were predicted numerically by a finite difference method. Rahman et al. [11] presented the transient analysis of a free jet of high Prandtl number fluid impinging on a stationary solid disk of finite thickness. Sarghini and Ruocco [12] presented a transient numerical analysis of a planar jet impingement on a finite thickness substrate at low volumetric flow rate including the effects of buoyancy. They found that conduction plays a very significant role at the initial part of the transient. Fang et al. [13] reported experimental measurements of transient mixed convection heat transfer characteristics of jet impingement onto a horizontally rotating ceramic–based multichip disk.

Although the above investigations provided very useful information, none has attempted to produce local heat transfer distribution for a rotating disk in combination with a partially confined liquid jet impingement. The present study attempts to carry out a comprehensive investigation of steady state and transient conjugate heat transfer analyses for liquid jet impingement over a spinning solid disk. The numerical model along with the results for steady and transient heat transfer for different Reynolds number, Ekman number, confinement ratio, disk thickness, and material properties are expected to be valuable towards the design of liquid jet impingement cooling or heating systems for various engineering applications.
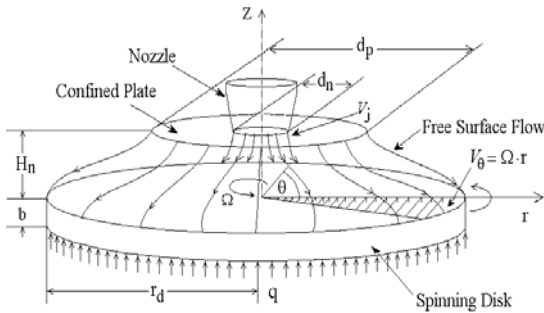
2. ANALYSIS AND COMPUTATION

Figure 1 Three dimensional schematic of axisymmetric semi-confined liquid jet impingement on a uniformly heated spinning disk
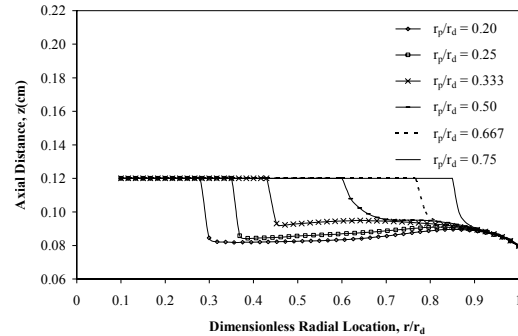

Figure 2 Free surface height distribution for different plate to disk confinement ratio with water as the cooling fluid (Re = 450, Ek = 4.25x10^{-4}, β=0.5, b/d$_n$ = 0.5)

A schematic of the physical problem is shown in figure 1. An axisymmetric liquid jet is discharged through a nozzle and impinges at the center of a solid uniformly heated circular disk. The top plate acts as an insulated partially confined boundary that ends allowing the exposure of the free surface boundary condition of the fluid. At t = 0, the power source is turned on and the heat starts to flow after an initially isothermal fluid flow has been established on the disk. The present study considers an incompressible flow of a Newtonian fluid. Due to rotational symmetry of the problem the $\partial/\partial\theta$ terms could be omitted. The equations describing the conservation of mass, momentum (r,θ and z directions respectively), and energy can be written as [14]:

$$\frac{\partial \rho_f}{\partial t} + \frac{1}{r}\frac{\partial}{\partial r}(\rho_f r V_r) + \frac{\partial}{\partial z}(\rho_f V_z) = 0 \tag{1}$$

$$\rho_f\left(\frac{\partial V_r}{\partial t} + V_r\frac{\partial V_r}{\partial r} + V_z\frac{\partial V_r}{\partial z} - \frac{V_\theta^2}{r}\right) = -\frac{\partial p}{\partial r} +$$

$$\frac{1}{r}\frac{\partial}{\partial r}\left[\frac{2}{3}\mu_f r\left(2\frac{\partial V_r}{\partial r} - \frac{V_r}{r} - \frac{\partial V_z}{\partial z}\right)\right] + \frac{\partial}{\partial z}\left[\mu_f\left(\frac{\partial V_r}{\partial z} + \frac{\partial V_z}{\partial r}\right)\right] + \frac{2}{3}\cdot\frac{\mu_f}{r}\left(\frac{\partial V_r}{\partial r} + \frac{\partial V_z}{\partial z} - \frac{2\cdot V_r}{r}\right) \tag{2}$$

$$\rho_f\left(\frac{\partial V_\theta}{\partial t} + V_r\frac{\partial V_\theta}{\partial r} + V_z\frac{\partial V_\theta}{\partial z} + \frac{V_r V_\theta}{r}\right) = \frac{1}{r^2}\frac{\partial}{\partial r}\left[r^2\mu_f\left(r\frac{\partial}{\partial r}\left(\frac{V_\theta}{r}\right)\right)\right] + \frac{\partial}{\partial z}\left[\mu_f\left(\frac{\partial V_\theta}{\partial z}\right)\right] \tag{3}$$

$$\rho_f\left(\frac{\partial V_z}{\partial t} + V_r\frac{\partial V_z}{\partial r} + V_z\frac{\partial V_z}{\partial z}\right) = -\rho_f g - \frac{\partial p}{\partial z} + \frac{1}{r}\frac{\partial}{\partial r}\left[r\mu_f\left(\frac{\partial V_r}{\partial z} + \frac{\partial V_z}{\partial r}\right)\right] + \frac{\partial}{\partial z}\left[\frac{2}{3}\mu_f\left(2\frac{\partial V_z}{\partial z} - \frac{V_r}{r} - \frac{\partial V_r}{\partial r}\right)\right] \tag{4}$$

$$\rho_f\left(\frac{\partial T_f}{\partial t} + V_r\frac{\partial(Cp_f T_f)}{\partial r} + V_z\frac{\partial(Cp_f T_f)}{\partial z}\right) = \frac{1}{r}\frac{\partial}{\partial r}\left(k_f r\frac{\partial T_f}{\partial r}\right) + \frac{\partial}{\partial z}\left(k_f\frac{\partial T_f}{\partial z}\right) +$$

$$2\cdot\mu_f\left[\left(\frac{\partial V_r}{\partial r}\right)^2 + \left(\frac{V_r}{r}\right)^2 + \left(\frac{\partial V_z}{\partial z}\right)^2 + \frac{1}{2}\left(\frac{\partial V_\theta}{\partial r} - \frac{V_\theta}{r}\right)^2 + \frac{1}{2}\left(\frac{\partial V_\theta}{\partial z}\right)^2 + \frac{1}{2}\left(\frac{\partial V_r}{\partial z} + \frac{\partial V_z}{\partial r}\right)^2 - \frac{1}{3}\left(\frac{\partial V_r}{\partial r} + \frac{V_r}{r} + \frac{\partial V_z}{\partial z}\right)^2\right] \tag{5}$$

The conservation of energy inside the solid can be characterized by the following equation:

$$\frac{\partial T_S}{\partial t} = \alpha_s\left[\frac{\partial^2 T_S}{\partial r^2} + \frac{1}{r}\left(\frac{\partial T_S}{\partial r}\right) + \frac{\partial^2 T_S}{\partial z^2}\right] \tag{6}$$

The following boundary conditions were used to complete the physical problem formulation.

At $r = 0$, $-b \le z \le 0$: $\dfrac{\partial T_S}{\partial r} = 0$ $\tag{7}$

At $r = 0$, $0 \le z \le H_n$: $V_\theta = V_r = 0, \dfrac{\partial V_z}{\partial r} = 0, \dfrac{\partial T_f}{\partial r} = 0$ $\tag{8}$

At $r = r_d$, $-b \le z \le 0$: $\dfrac{\partial T_S}{\partial r} = 0$ $\tag{9}$

At $r = r_d$, $0 \le z \le \delta$: $p = p_{atm}$ $\tag{10}$

At $z = -b$, $0 \le r \le r_d$: $-k_s\dfrac{\partial T_s}{\partial z} = q_w$ $\tag{11}$

At $z = 0$, $0 \le r \le r_d$: $V_r = V_z = 0$, $V_\theta = \Omega\cdot r$, $T_f = T_S$, $k_s\dfrac{\partial T_S}{\partial z} = k_f\dfrac{\partial T_f}{\partial z}$ $\tag{12}$

At $z = H_n$, $0 \le r \le r_n$: $V_z = -V_j, V_r = V_\theta = 0$, $T_f = T_j$ $\tag{13}$

At $z = H_n$, $r_n \le r \le r_p$: $V_r = V_z = V_\theta = 0$, $\dfrac{\partial T_f}{\partial z} = 0$ $\tag{14}$

The boundary condition at the free surface after confinement can be expressed as:

At $z = \delta$, $r_p \le r \le r_d$:

$$\frac{\partial \delta}{\partial r} = \frac{V_z}{V_r}, p = p_{atm} - \frac{\sigma\dfrac{d^2\delta}{dr^2}}{\left[1 + \left(\dfrac{d\delta}{dr}\right)^2\right]^{3/2}}, \frac{\partial V_s}{\partial n} = 0, \frac{\partial T_f}{\partial n} = 0 \tag{15}$$

where V_S is the fluid velocity component along the free surface and n is the coordinate normal to the free surface. In the absence of any significant resistance from the ambient gas, the shear stress encountered at the free surface is essentially zero. Similarly, a negligible heat transfer at the free surface results in zero temperature gradient.

The solid disk was assumed to be at thermal equilibrium with jet fluid before the heating of the plate was turned on. The velocity field at this condition was determined by solving only the continuity and momentum equations in the fluid region. Thus,

At t = 0: $T_f = T_s = T_j$, $\vec{V_i} = \vec{V}\left(\text{isothermal}\right)$ (16)

The average heat transfer coefficients can be defined as:

$$h_{av} = \frac{2}{r_d^2 \cdot \left(\overline{T}_{int} - T_j\right)} \int_0^{r_d} hr\left(T_{int} - T_j\right) dr$$ (17)

where $\overline{T}_{int}$ is the average temperature at the solid–fluid interface.

The governing equations (1–6) along with the boundary and initial conditions (7–16) were solved using the Galerkin finite element method [15]. Four node quadrilateral elements were used. In each element, the velocity, pressure, and temperature fields were approximated which led to a set of equations that defined the continuum. The number of elements required for accurate results was determined from a grid independence study. The size of the elements near the solid-fluid interface was made smaller to adequately capture large variations in velocity and temperature in that region. In order to determine the initial velocity field (V_i), the equations for the conservation of mass and momentum were solved. Since the solution of the momentum equation required only two out of the three boundary conditions at the free surface, the third condition that relates the slope of the free surface to local velocity components at the free surface was used to upgrade the position of the free surface at the end of each iteration step. The solver used spines to track the free surface and re–arranged grid distribution with the movement along the free surface. The spines are straight lines passing through the free surface nodes and connect the remaining nodes underneath the free surface. The movement of the free surface affected only the nodes along the spine. Once the final free surface height distribution and the flow–field for the isothermal equilibrium condition were reached, the power was turned on and heat began to flow. Then the computation domain included both solid and fluid regions. The continuity, momentum, and energy equations were solved simultaneously as a conjugate problem taking into account the variation of fluid properties with temperature. The computation covered the entire transient period all the way to the steady state condition. Because of large changes at the start of the transient and very small changes when the solution approached the steady–state condition, a fixed time step was used to cover the earlier part of the transient up to 25 s, and a variable time step was used for the rest of the computation. At each time step, the solution was considered converged when relative change in field values from a particular iteration to the next, and the sums of the residuals for each variable became less than 10^{-6}.

For numerical computation, the nozzle opening and the heated target disk had radii of 0.6 and 6.0 mm respectively. The heat flux (q) was kept constant at 125 kW/m^2. The incoming fluid jet temperature (T_j) was 310 K for water and FC–77, 303K for ammonia (at a pressure of 20 bars), and 373 K for MIL–7808. The spinning rate (Ω) was varied from 0 to 78.54 rad/s or 0 to 750 rpm. The flow rate was varied from 6.65×10^{-7} to 2.72×10^{-6} m^3/s. These provided the range for Reynolds and Ekman numbers of Re = 220-900 and Ek = 7.08×10^{-5}- ∞. The possibility of getting into turbulent flow regime was checked using the laminar–turbulent transition criterion used by Popiel and Boguslawski [16] and Vanyo [17]. All runs used in the paper checked out to be laminar. A comparison of average heat transfer coefficient was done with the experimental data of Carper and Deffenbaugh [3] and Carper et al. [4]. The agreement was found to be quite good. In addition, a comparison of local Nusselt numbers

was made with the experimental data obtained by Ozar et al. [8] at various rotational speeds. The difference was in the range of 0.79 to 22.07 % with an average difference of 12.33 %.

3. RESULTS AND DISCUSSION

Figure 2 presents the free surface height distribution for different plate to disk confinement ratio when the jet strikes the center of the disk while it is spinning at a rate of 125 rpm (Ek = 4.25×10^{-4}). It can be seen that the fluid spreads out radially as a thin film. The film thickness decreases as the plate to disk confinement ratio decreases under the same spinning rate and flow rate. This behavior occurs due to dominance of surface tension and gravitational forces that form the free surface as the fluid leaves the confinement zone and moves downstream. When r_p is increased, the frictional resistance from both walls slows down the momentum and results in higher film thickness. For the conditions considered in the present investigation, a sudden drop in fluid height occurs for $r_p/r_d < 0.333$ because the equilibrium film height for free surface motion is significantly lower than confinement height. In this situation, liquid may not cover all the way to the end of the confinement disk and free surface may start to form within the confinement region to provide a smooth streamline for the free surface. At $r_p/r_d \geq 0.5$, the confinement region is fully covered with fluid and a smooth transition is seen in film height distribution after exit.

Figure 3 shows the local Nusselt number and the dimensionless interface temperature variation for different Reynolds number under a rotational rate of 125 rpm (Ek = 4.25×10^{-4}). The dimensionless interface temperature decreases with jet velocity (or Reynolds number). At any Reynolds number, the dimensionless interface temperature has the lowest value at the stagnation point (underneath the center of the axial opening) and increases radially downstream reaching the highest value at the end of the disk. This is due to the development of thermal boundary layer as the fluid moves downstream from the center of the disk. The thickness of the thermal boundary layer increases with radius and causes the interface temperature to increase. All local Nusselt number distributions are half–bell shaped with a peak at the stagnation point.
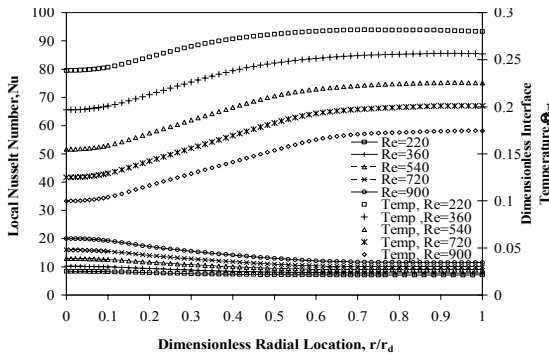

Figure 3 Local Nusselt number and dimensionless interface temperature distributions for a silicon disk with water as the cooling fluid for different Reynolds numbers (Ek = 4.25×10^{-4}, $\beta = 0.5$, b/d_n = 0.5, $r_p/r_d = 0.667$)
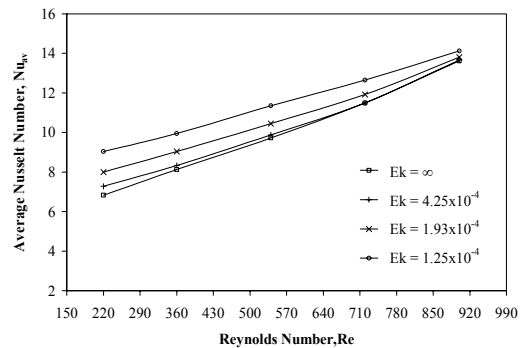
Figure 4 Average Nusselt number variations with Reynolds number at different Ekman numbers for a silicon disk with water as the cooling fluid ($\beta = 0.5$, b/d_n = 0.5, $r_p/r_d = 0.667$)

Figure 4 plots the average Nusselt number as a function of Reynolds number for low, intermediate, and high Ekman numbers. It may be noted that average Nusselt number increases with Reynolds number. As the flow rate or Reynolds number increases, the magnitude of fluid velocity near the solid-fluid interface that controls the convective heat transfer rate increases. Furthermore, at a particular Reynolds number, the Nusselt number

gradually increases with the increment of disk spinning rate. This behavior confirms the positive influence of the rotational rate on the average Nusselt number down to Ek=1.25x10^{-4} that corresponds to a spinning rate of 425 rpm. It may be also noticed that the average Nusselt number plots get closer to each other as the Reynolds number increases indicating that curves will intersect at higher Reynolds numbers. These intersections indicate the presence of a liquid jet momentum dominated region at higher Reynolds numbers. From the numerical results it was observed that the heat transfer is dominated by impingement when Re·Ek>0.124 and dominated by disk rotation when Re·Ek<0.092. In between there limits, both of these effects play important roles in determining the variations of average Nusselt number.
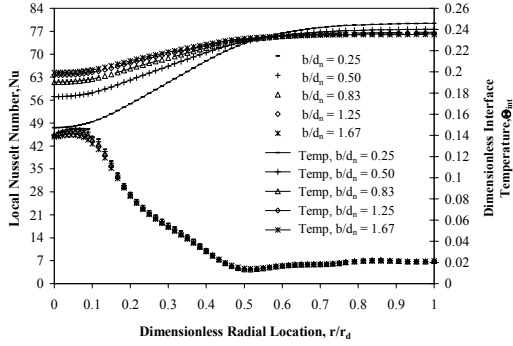

Figure 5 Local Nusselt number and dimensionless interface temperature distributions for different silicon disk thicknesses with water as the cooling fluid (Re = 450, Ek = 4.25x10^{-4}, β = 0.5, r_p/r_d = 0.667)
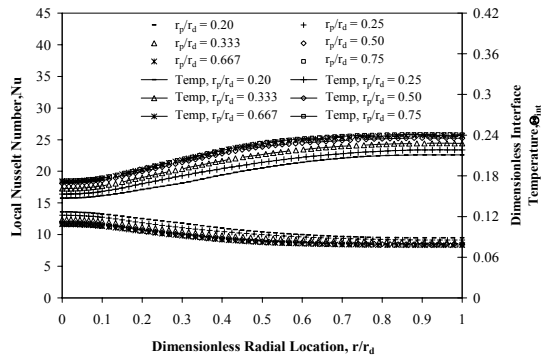
Figure 6 Local Nusselt number and interface temperature distributions for different plate to disk confinement ratios with water as the cooling fluid (Re = 450, Ek = 4.25x10^{-4}, β = 0.5, b/d_n = 0.5)

The effects of disk thickness variation on the dimensionless interface temperature and local Nusselt number are shown in figure 5. The dimensionless interface temperature increases from the impingement region all the way to the end of the disk. It may be noted that the curves intersect with each other at a dimensionless radial distance of r/r_d=0.55. The thicker disks generate more uniform dimensionless interface temperature due to larger radial conduction within the disk. The local Nusselt number plots change slightly with the variation of disk thickness. In all cases, it is evident that the Nusselt number is more sensitive to solid thickness at the core region where higher values are obtained. For a lower stagnation temperature, the outlet temperature tends to be relatively higher under constant flow rate and heat flux conditions. This is quite expected because of the overall energy balance of the system. This phenomenon has also been documented by Lachefski et al. [18].

Six different plate–to–disk confinement ratios (r_p/r_d) from 0.2 to 0.75 were modeled for water as the coolant and silicon as the disk material. The effects of plate–to–disk confinement ratio on the dimensionless interface temperature and local Nusselt number are shown in figure 6. The dimensionless interface temperature increases with the increment of the plate–to–disk confinement ratio (r_p/r_d). This increment coincides with the increment of liquid film thickness in the free jet region as seen in figure 2. Under the same spinning and flow rates, when r_p is increased the higher frictional resistance from the confinement disk slows down the fluid momentum. In addition, a thinner film thickness for the same flow rate results in higher fluid velocity near the solid–fluid interface resulting in a higher rate of convective heat transfer. This is seen in the distribution of local Nusselt number which increases with the decrease of plate–to–disk confinement ratio.

Figure 7 compares the dimensionless interface temperature and local Nusselt number results of the present working fluid (water) with three other coolants, namely ammonia (NH$_3$), flouroinert (FC–77) and oil (MIL–7808) under a Reynolds number of 750. Even though the

rotational rate (Ω) for the impingement disk was set at 350 rpm the variation of Ekman number occurred since the density (ρ) and dynamic viscosity (μ) are different for each fluid. It may be noticed that MIL–7808 presents the highest dimensionless interface temperature and water has the lowest value. Ammonia shows the most uniform distribution of temperature along the radius of the disk. MIL–7808 presents the highest local Nusselt number values over the entire radial distance. Ammonia on the other hand provides the lowest Nusselt number. Higher Prandtl number fluids lead to a thinner thermal boundary layer and therefore more effective heat removal rate at the interface. Present working fluid results are in agreement with Li et al. [19] findings where a larger Prandtl number corresponded to a higher recovery factor.

Figure 8 shows the dimensionless interface temperature and local Nusselt number distribution plots as a function of dimensionless radial distance (r/r_d) measured from the axisymmetric impingement axis for different solid materials with water as the working fluid. Constantan shows the lowest temperature at the impingement zone and the highest temperature at the outlet in comparison with other solid materials. Copper and silver show a more uniform distribution and higher temperature values at the impingement zone due to their higher thermal conductivity. The dimensionless temperature and local Nusselt number distributions of these two materials are almost identical due to their similar thermal conductivity values. The cross-over of curves for all five materials occurred due to a constant fluid flow and heat flux rate that reaches a thermal energy balance. A solid material with lower thermal conductivity shows higher maximum local Nusselt number.
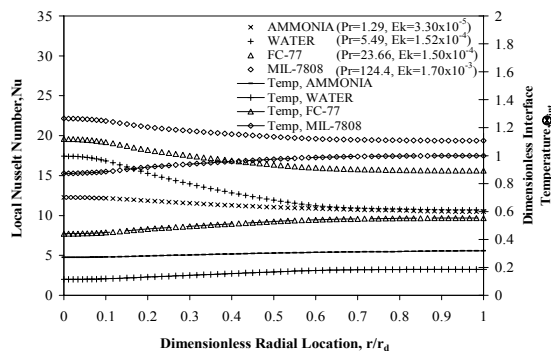

Figure 7 Local Nusselt number and dimensionless interface temperature distributions for different cooling fluids for silicon as the disk material (Re = 750, β = 0.5, b/d_n = 0.5, r_p/r_d = 0.667)
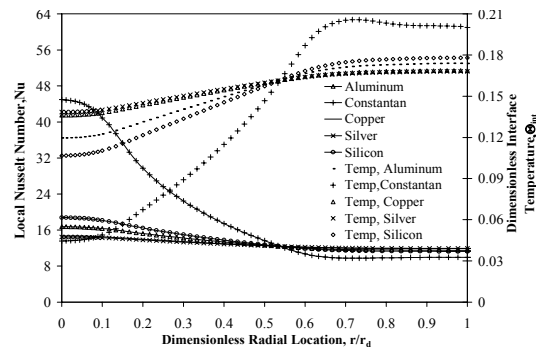
Figure 8 Local Nusselt number and interface temperature distributions for different solid materials with water as the cooling fluid (Re = 875, Ek = 4.25x10^{-4}, β = 0.5, b/d_n = 0.5, r_p/r_d = 0.667)

The integrated average Nusselt number and the variation of dimensionless maximum temperature at the interface, maximum temperature inside the solid, and maximum–to–minimum temperature difference at the interface at different Fourier numbers are shown in Fig. 9. The average Nusselt number is large at the early part of the transient and monotonically decreases with time ultimately reaching the value for the steady state condition. A higher Reynolds number increases the magnitude of fluid velocity near the solid–fluid interface that controls the convective heat transfer and therefore increases the average Nusselt number. The control of maximum temperature is important in many critical thermal management applications including electronic packaging. As expected, the temperature increases everywhere with time starting from the initial isothermal condition. A rapid increment is seen at the earlier part of the transient, and it levels off as the thermal storage capacity of the solid diminishes and become zero at the steady state condition. The

maximum–to–minimum temperature difference at the interface increases with time as more heat flows through the solid disk and transmitted to the fluid.
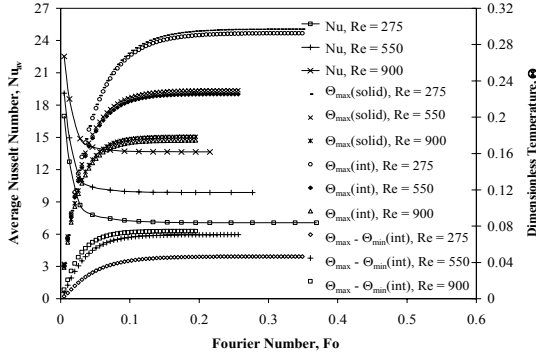

Figure 9 Average Nusselt number and temperature variations at the interface, inside the solid, and maximum–to–minimum temperature difference at the interface at different Fourier numbers with water as the cooling fluid for various Reynolds numbers (Ek=4.25x10^{-4}, β=0.5, b/d$_n$= 0.5,and r$_p$/r$_d$=0.667).
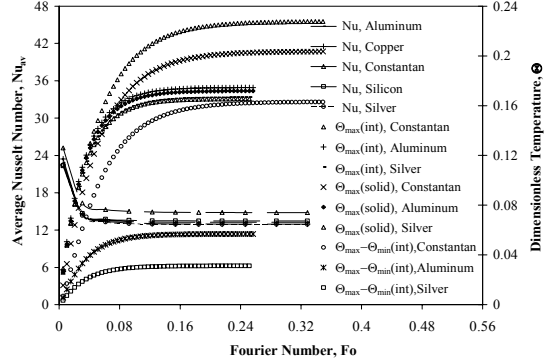
Figure 10 Average Nusselt number variations and temperature variation at the interface, inside the solid, and maximum–to–minimum interface temperature difference at different Fourier numbers with water as the cooling fluid for different solid materials (Re=875, Ek=2.13x10^{-4}, b/d$_n$=0.5, β=0.5, and r$_p$/r$_d$ = 0.667).

The effects of solid material properties on transient heat transfer are presented in Fig. 10. The temperature changes occur faster at the earlier part of the heating process and the slope gradually decays when the steady–state condition approaches. It can be observed that a material having a lower thermal conductivity such as Constantan maintains a higher temperature and average heat transfer coefficient over the entire transient process as the thermal conductivity controls how effectively the heat flows and distributes through the material. For the same reason, the maximum temperature within the solid and that at the interface are significantly different for Constantan, whereareas about the same for both silver and aluminum. The thermal diffusivity of the solid plays a significant role in determining the duration of the transient heat transfer process. Constantan takes longer in reaching steady–state due to its lower thermal diffusivity compared to the other materials. The magnitude of the temperature non–uniformity at the interface at steady state is controlled by thermal conductivity of the material. It may be noted that Constantan (k$_{Constantan}$=22.7 W/m·K) has an average maximum–to–minimum temperature difference of 17.24 K, whereas silver (k$_{silver}$=429 W/m·K) has only an average 3.34 K temperature difference at the interface. It is also important to know how the materials responded in reaching thermal equilibrium based on their thickness. As the thickness increases, the time to reach steady–state also increases. The radial conduction becomes stronger as the disk thickness increases generating a more uniform temperature distribution at the interface. However, the increment of solid thickness creates more thermal resistance to the heat transfer process.

4. CONCLUSIONS

The solid–fluid dimensionless interface temperature and local Nusselt number showed a strong dependence on Reynolds number, rotational rate, disk thickness, plate–to–disk confinement ratio, fluid properties, and solid material properties. Both flow rate and spin rate of the target disk increase the local heat transfer coefficient distribution over the entire solid-fluid interface. A higher disk thickness provides a more uniform distribution of interface

8

temperature and heat transfer coefficient. A decrease in plate to disk confinement ratio increases the local Nusselt number at all locations in the disk. A higher Prandtl number fluid leads to a thinner thermal boundary layer and provides a more effective heat removal rate at the interface. Plate materials with higher thermal conductivity maintain a lower thermal resistance within the solid and therefore a more uniform temperature distribution happens at the interface. The dimensionless interface temperature increases and Nusselt number decreases with the progression of the transient from the start–up of heating to the equilibrium steady–state condition. It was detected that the time for the plate to achieve the steady–state condition increased with disk thickness and decreased with Reynolds number and thermal conductivity ratio.

5. NOMENCLATURE

b   disk thickness [m]

C_p specific heat [J/kg–K]

d   diameter [m]

Ek   Ekman number, $\nu_f/(4 \cdot \Omega \cdot r_d^2)$

F_o Fourier number, $\alpha_f t/ d_n^2$

g   acceleration due to gravity [m/s^2]

h   heat transfer coefficient [W/m^{2}K], $q_{int}/(T_{int}–T_j)$

h_{av} average heat transfer coefficient [W/m^{2}K], defined by equation (17)

H_n distance of nozzle to the plate [m]

k   thermal conductivity [W/m K]

Nu   Nusselt number, $(h \cdot d_n)/k_f$

Nu_{av} average Nusselt number, $(h_{av} \cdot d_n)/k_f$

p   pressure [Pa]

Pr   Prandtl number, $(\mu_f \cdot Cp_f)/ k_f$

Greek letters

α thermal diffusivity [m^2/s]

β nozzle-to-target spacing, H_n/d_n

δ free surface height [m]

ε thermal conductivity ratio, k_S/k_f

μ dynamic viscosity [kg/m–s]

ν kinematic viscosity [m^2/s]

Subscripts

atm   ambient

av   average

f   fluid

i   initial condition

int   interface

j   jet or inlet

q   heat flux [W/m^2]

r   radial coordinate [m]

r_d disk radius [m]

r_p plate radius [m]

r_p/r_d Confinement ratio

Re   Reynolds number, $(V_j \cdot d_n)/\nu_f$

t   time [s]

T   temperature [K]

$\overline{T}_{int}$ average interface temperature [K],

$$\frac{2}{r_d^2}\int_0^{r_d} T_{int}\, r dr$$

V_j jet velocity [m/s]

$V_{r, z, \theta}$ velocity component in the r, z and θ–direction [m/s]

z   axial coordinate [m]

θ angular coordinate [rad]

Θ dimensionless temperature, $2 \cdot k_f (T_{int}–T_j)/(q_w \cdot d_n)$

ρ density [kg/m^3]

σ surface tension [N/m]

Ω angular velocity [rad/s]

max   maximum

n   nozzle

p   plate

s   solid

w   bottom surface of impingement disk

6. REFERENCES

[1]   Watson, E.J., The Radial Spread of a Liquid Jet Over a Horizontal Plane, Journal of Fluid Mechanics, 20 (1964), 3, pp. 481–499.

[2] Polat, S., Huang, B., Mujumdar, A.S., Douglas, W.J.M., Numerical Flow and Heat Transfer Under Impinging Jets: A review, Annual Review Numerical Fluid Mechanics and Heat Transfer, 2 (1989), 2, pp. 157–197.

[3] Carper Jr., H.J., Deffenbaugh, D.M., Heat Transfer From a Rotating Disk with Liquid Jet Impingement, 6th International Heat Transfer Conference, Toronto, Canada, Hemisphere Public Corp, Washington, DC, Vol.4, 1978, pp. 113–118.

[4] Carper Jr., H.J, Saavedra, J.J., Suwanprateep, T., Liquid Jet Impingement Cooling of a Rotating Disk, Journal of Heat Transfer, 108 (1986), 3, pp. 540–546.

[5] Metzger, D.E., Bunker, R.S., Bosh, G., 1991, Transient Liquid Crystal Measurement of Local Heat Transfer on a Rotating Disk with Jet Impingement, Journal of Turbomachinery, 113, (1991), 1, pp. 52 – 59.

[6] Thomas, S., Faghri, A., Hankey, W.L., Experimental Analysis and Flow Visualization of a Thin Liquid Film Over on a Stationary and Rotating Disk, Journal of Fluids Engineering, 113 (1991), 1, pp. 73–80.

[7] Hung, Y.H., Shieh, Y.R., Convective Heat Transfer From a Rotating Ceramic–based Multichip Disk with Round Jet Impingement, Proc. National Heat Transfer Conference, Anaheim, CA, Vol. 1, 2001, pp. 97–103.

[8] Ozar, B., Cetegen, B.M., Faghri, A., Experiments on Heat Transfer in a Thin Liquid Film Flowing Over a Rotating Disk, Journal of Heat Transfer, 126 (2004), 2, pp. 184–192.

[9] Rice, J., Faghri, A., Cetegen, B.M., Analysis of a Free Surface Film From a Controlled Liquid Impinging Jet Over a Rotating Disk Including Conjugate Effects, with and without Evaporation, Inter. Journal of Heat and Mass Transfer, 48 (2005), 25–26, pp. 5192–5204.

[10] Fujimoto, H., Takuda, H., Hatta, N., Viskanta, R., Numerical Simulation of Transient Cooling of a Hot Solid by an Impinging Free Surface Jet, Numerical Heat Transfer, Part A, 36 (1999), 8, pp. 767–780.

[11] Rahman, M.M., Bula–Silvera, A.J., Leland, J.E., Analysis of Transient Conjugate Heat Transfer to a Free Impinging Jet, Journal of Thermophysics and Heat Transfer, 14 (2000), 3, pp. 330–339.

[12] Sarghini, F., Ruocco, G., Enhancement and Reversal Heat Transfer by Competing Modes in Jet Impingement, Inter. Journal of Heat and Mass Transfer, 47 (2004), 8–9, pp. 1711–1718.

[13] Fang, C. J., Wu, M.C., Kuo, Y.M., Lee, C.Y., Peng, C. H., Hung, Y.H., Heat Transfer Behavior for a Stationary or Rotating MCM Disk With an Unconfined Round Jet Impingement, Journal of Electronic Packaging, 129 (2007), 4, pp. 400–410.

[14] Burmeister, L.C., Convective Heat Transfer, 2nd ed. John Wiley and Sons Inc, NY, 1993.

[15] Fletcher, C.A.J., Computational Galerkin Methods, Springer Verlag, NY, 1984.

[16] Popiel, C.O., Boguslawski, L., Local Heat Transfer from a Rotating Disk in an Impinging Round Jet, Journal of Heat Transfer, 108 (1986), 2, pp. 357 – 364.

[17] Vanyo, J.P., Rotating Fluids in Engineering and Science, Butterworth–Heinemann, MA, 1993.

[18] Lachefski, H., Cziesla, T., Biswas, G., Mitra, K., Numerical Investigation of Heat Transfer by Rows of Rectangular Impinging Jets, Numerical Heat Transfer, Part A, 30 (1996), 1, pp. 87–101.

[19] Li, D.Y., Guo, Z.Y., Ma, C.F., Relationship Between the Recovery Factor and the Viscous Dissipation in a Confined Impinging Circular Jet of High–Prandtl Number Liquid, Inter., Journal of Heat and Fluid Flow, 18 (1997), 6 , pp. 585–590.

HEAT TRANSFER ENHANCEMENT AND PRESSURE DROP IN MICROFIN TUBES

Akio Miyara

Department of Mechanical Engineering, Saga University
1 Honjomachi, Saga-Shi, 849-8502, Japan
Email: miyara@me.saga-u.ac.jp

ABSTRACT

Microfin tubes have been exclusively used to enhance heat transfer of condensation and evaporation of refrigerant flowing in tube because they improve the heat transfer with small increase of pressure loss. In air-conditioners and refrigeration systems, efficient heat exchangers which have high heat transfer coefficient and low pressure loss contribute to higher system performance. Since the first microfin tube was developed in 1977, many types of microfins have been produced and the heat transfer performance has risen. Shape of the first microfin was triangular and the heat transfer coefficient was about two times of smooth tube. The shape changed to trapezoid both the fin and groove formed between fins. After the change, the fin shape was upgraded and the heat transfer coefficient becomes three times. In the middle of 1990's, new types of microfins, such as herringbone and cross grooved, were developed. Effects of the microfins on heat transfer enhancement are (1) augmentation of heat transfer area, (2) Generation of turbulence, (3) thinning of liquid film, and (4) feed of liquid. In the case of single phase flow the area augmentation and turbulence generation are effective. On the other hand, the film thinning and liquid feed are dominant for the condensation and evaporation two phase flow. The enhancement efficiency depends on flow conditions and the enhancement mechanisms differ between condensation and evaporation. In this paper, brief history of the microfin tube is mentioned and the heat transfer enhancement mechanism is explained. Correlations for pressure loss and heat transfer coefficient are also introduced.

Keywords: *Microfin tube, Heat transfer, Pressure loss, Condensation, Evaporation.*

1. INTRODUCTION

In air-conditioners and refrigeration systems, heat exchangers have important functions on the system performance. Under a constant refrigeration capability condition, higher heat transfer coefficient makes smaller pressure ratio of condenser to evaporator and yields higher coefficient of performance (COP). It also makes reduction of heat exchanger materials. Low pressure losses of refrigerant side and air side in heat exchangers reduce required electric powers of compressor and fan, respectively, and raise the COP. Therefore, heat exchangers which have high heat transfer performance and low pressure loss are desired.

Fin-tube heat exchangers have been used for the heat exchange between refrigerant and air as shown in Fig.1. In the fin-tube heat exchanger, heat transfer resistances are the convective heat transfer resistance of refrigerant flowing in tube, where refrigerant is condensing or evaporating, the contact resistance between tubes and fins, and the convective resistance of air flowing through fins. Because the heat transfer ability of air is very low in comparison with that of condensing or evaporating refrigerant in the tube, many fins are installed around tubes to increase the heat transfer area. It is said that the degrees of thermal resistances are 70~75% for air-side, 15~20% for refrigerant side, and 10~15% for thermal contact of tube and fin. In the last decades, the efforts have been poured into development of convection heat transfer enhancement for both sides. Although the resistance of air side is relatively larger than that of

refrigerant side, heat transfer enhancement of refrigerant side has been also required because air side heat transfer has been considerably enhanced by wavy, louver, and offset fins. The heat transfer enhancements of condensing and evaporating refrigerant have been exclusively achieved by microfin tubes, which are also called as internally grooved tubes, because they give considerable improvement of heat transfer coefficient accompanying small increase of pressure loss. On the other hand, inserts such as twisted tape and mixing devices induce large pressure loss though heat transfer is enhanced.
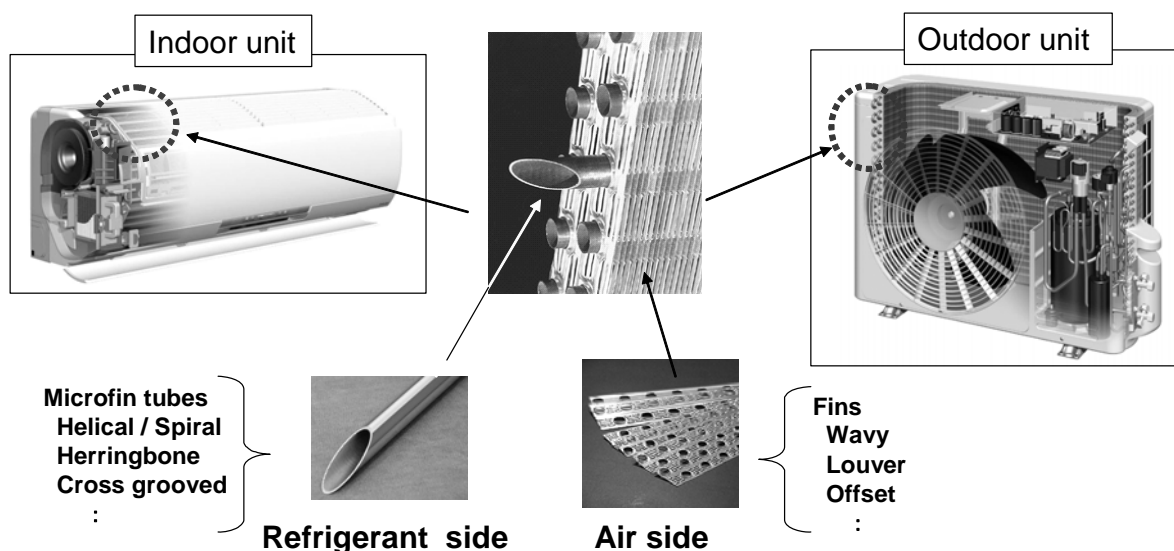

Fig. 1 Fin-tube heat exchangers in air-conditioners. (Courtesy of Hitachi, Ltd)

In this paper, historical development of microfin tubes is briefly mentioned first and then heat transfer enhancement mechanism is explained. Characteristics and correlations of pressure loss and heat transfer coefficient for single phase flow, condensation, and evaporation are also presented.

2. HISTORICAL DEVELOPMENT OF MICROFIN TUBES

Figs. 2 (a) and (b) show changes of heat transfer enhancement rate of condensation and evaporation in microfin tubes, respectively. Where the values indicate outlines and the enhancement rates change very much depending on flow conditions, which are mass velocity and vapor quality. Changes of the fin and groove shape are also illustrated accompanied with the enhancement variation. First development of the microfin tube was accomplished by a Japanese company [1] in 1977. One of the innovators, Itoh [2], reported that the original microfin tube was accidentally produced from a limitation of process forming high fin inside a copper tube, where originally designed high inner fins were changed to very small fins and grooves between fins. In Japan, the microfin tube is mainly called as "helically grooved tube", which is literal translation of Japanese. Probably, first they looked like grooves rather than fins. After the first innovation, many kinds of micorfin tubes have been developed. Fin and groove profile of first generation is sinusoidal or triangular shape. For next generation, fins and grooves changed to trapezoidal shape and then fin becomes slim and high. In the middle of 1990s, cross grooved microfin tubes and herringbone microfin tubes are produced. The herringbone microfin tube have 2~3 V-shape fins which makes herringbone pattern.

On the other hand, tube diameter changed form 9.52mm to 7mm in 1980s. In 1990s, tubes with outer diameter of 7mm were mainly used. So far, tube diameter continues to decrease and tubes with smaller diameter such as 5mm of outer diameter are partly used in heat exchangers.

These transitions of tube diameter have been carried out in order to reduce fan power for air flow and to get higher heat transfer performance. In recent years, reduction of refrigerant charged in the systems is also required because of global warming by refrigerants which would be released from the system. For the reduction, smaller diameter tube would be used more in the future.
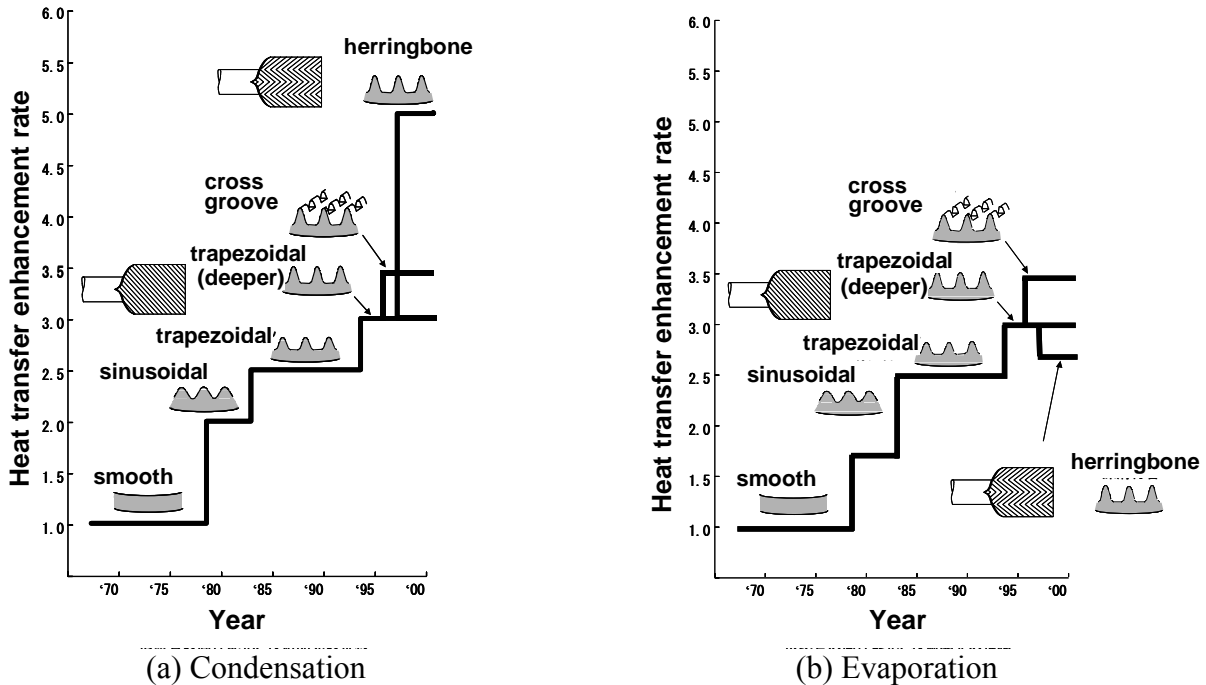

(a) Condensation   (b) Evaporation

Fig. 2 Historical development of microfin tubes and heat transfer enhancement rate.

3. HEAT TRANSFER ENHANCEMENT MECHANISM

There are mainly four kinds of effect of microfins on heat transfer enhancement, such as (1) augmentation of heat transfer area, (2) Generation of turbulence, (3) thinning of liquid film, and (4) feed of liquid. The heat transfer enhancement mechanism differs with flow conditions.

In the case of single phase flow the area augmentation and turbulence generation enhance the heat transfer. Since the fin height is comparable order with thickness of viscous sub-layer although it is depending on the Reynolds number, both the enhancement effects would be comparably dominant. According to experiments [3], the heat transfer coefficient of helical microfin tubes becomes almost same as smooth tube in low Reynolds number condition of Re<6000, although it shows higher value in higher Reynolds number region. In the low Reynolds number condition, the boundary layer thickness might be larger than fin height.

Although the film thinning effect plays the important role on the enhancement of condensation and evaporation, the action of the film is somewhat different. As shown in Fig. 3, the condensate covers the entire fin surface and the film becomes thinner around corner of the microfin [4] because the condensate is drawn into bottom of groove by the surface tension effect. Larger heat transfer is achieved at the thin film area. On the other hand, meniscus film is formed in the groove and very thin films exist at the tips of the meniscus film and the evaporation is very active at the tip of film [5]. Liquid is supplemented to the tips by the surface tension effect. Cross grooved microfin tube was produced in order to increase the thin film part.
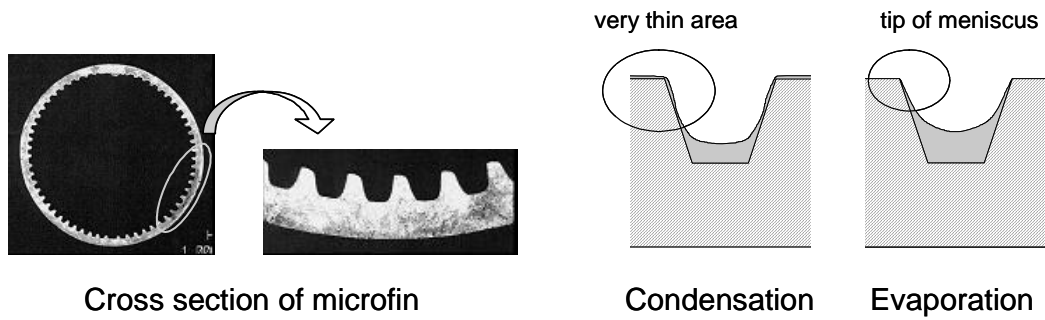
Cross section of microfin   Condensation   Evaporation

Fig. 3 Cross section of a microfin tube and liquid film around microfin.

Figs. 4 and 5 show typical flow patterns of condensation and evaporation in a smooth tube for low and high mass velocity conditions, respectively. Effects of the liquid feed differ depending on the flow pattern and type of microfins. Helical microfins generate helical flow [6] which feed liquid from bottom to top of the tube and flow pattern transition to annular flow occur lower quality and lower mass velocity than those of smooth tube. This liquid feed to tube top is very effective to avoid dryout in the low mass velocity condition. It is also said that liquid is drawn up to tube top by capillary effect trough the grooves even if the helical flow does not occur under the condition that the mass velocity is very small and vapor shear stress is negligible. On the other hand, in the case of high mass velocity, earlier transition to annular flow creates thick film around the entire inner surface as covering the fins. Because the liquid overflows the grooves and the thin film parts disappear, heat transfer is not so enhanced.
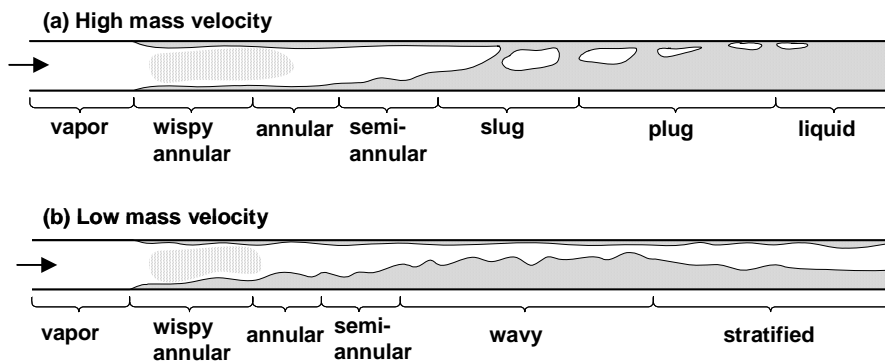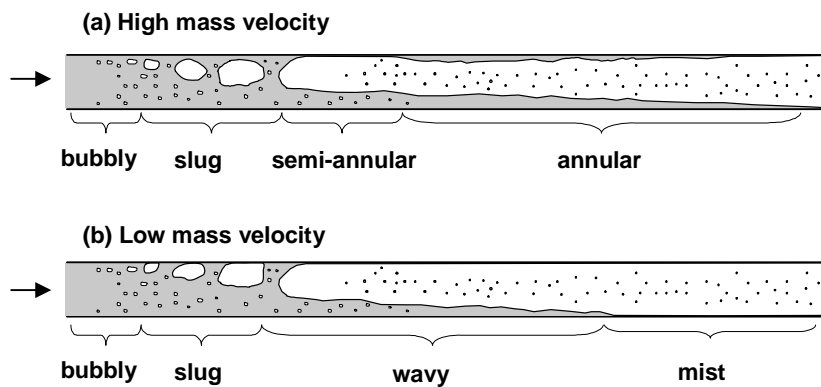

Fig. 4 Flow patter of condensed liquid.

Fig. 5 Flow patter of evaporating liquid.

Herringbone microfins have different liquid feed mechanism [7]. As shown in Fig.6, herringbone microfins work to remove liquid at fin-diverging parts and collect liquid at fin converging parts. When the fin-converging parts are set on tube top and bottom, liquid is corrected to the tube top and bottom (Fig.6(a)). On both sides of the tube, liquid is removed. In Fig. 7, heat transfer coefficient of condensation and evaporation are shown [8,9]. Fin geometries are in Table 1. In the case of condensation, microfins remove condensed liquid and keep very thin film. Therefore the heat transfer coefficients are higher than those of smooth and helical microfin tubes. On the other hand, in the case of evaporation, the liquid removal would cause lack of liquid and start earlier dryout. Some experimental results show decrease of heat transfer coefficient caused by the early dryout. However, the evaporation heat transfer coefficient of the herringbone tube shows higher than that of the helical microfin tube when the refrigerant mass velocity is sufficiently large and tube has suitable fin shape. The reason is that considerable droplets are entrained into vapor flow and four circulation flow generated by herringbone fins convey the droplets to tube side and the dryout is avoided. Fig. 8(a) shows ratio of droplet to total liquid flow rate and Fig. 8(b) illustrates four circulation flows which are obtained by a numerical simulation [7].

(a) flow induced by microfins   (b) liquid distribution   (c) liquid flow observation
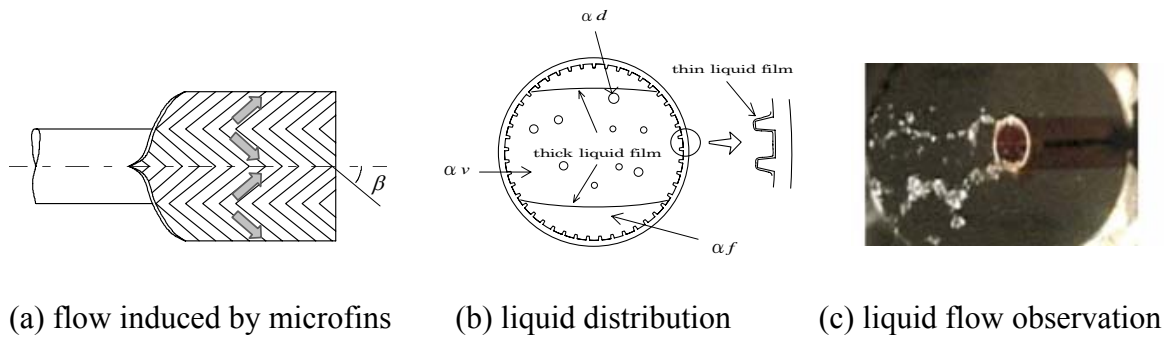
Fig. 6 Flow configuration of liquid in herringbone micorofin tube.

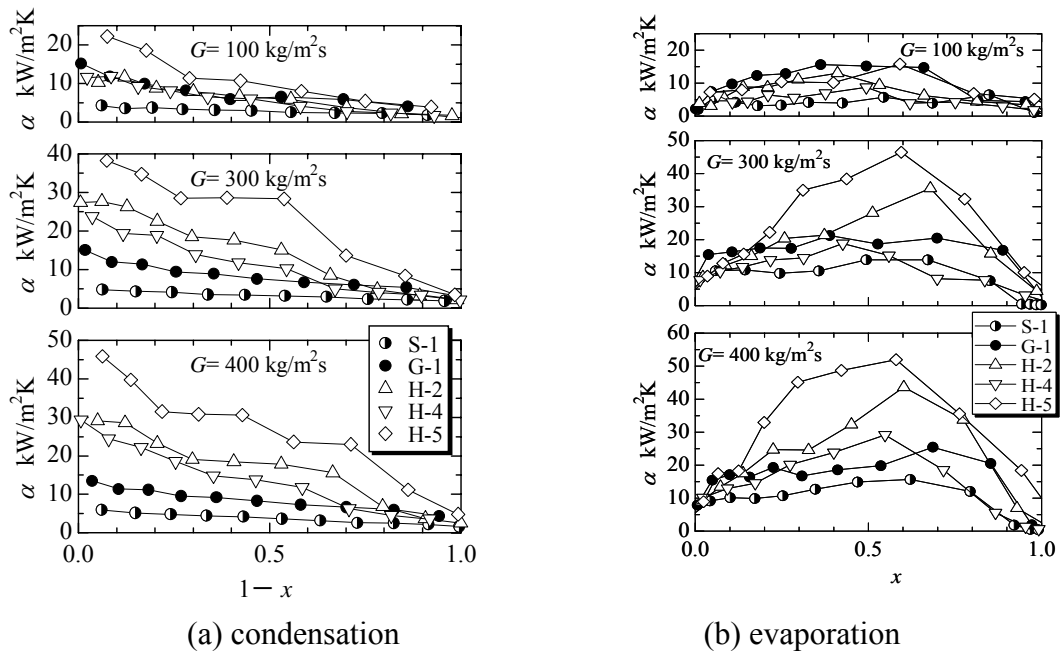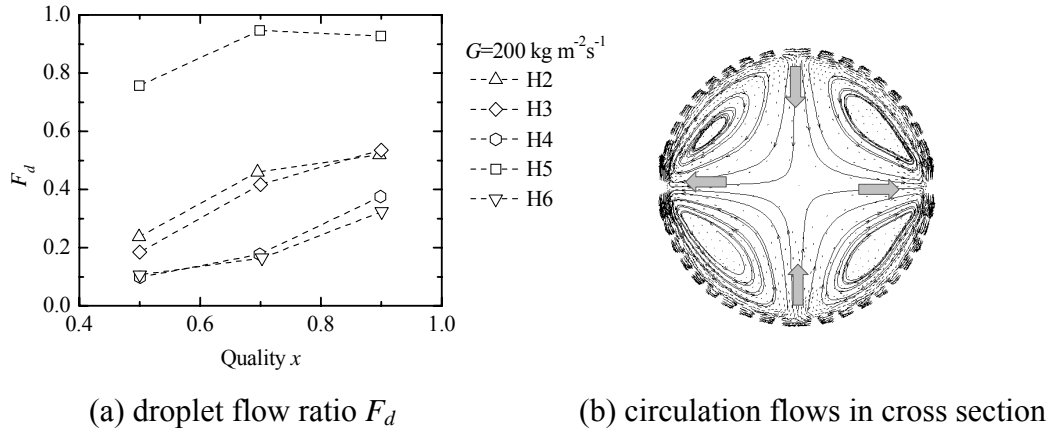(a) condensation   (b) evaporation

Fig. 7 Heat transfer coefficients of smooth tube, helical and herringbone microfin tube.
(S: smooth, G: helical microfin, H: herringbone microfin)

Table 1 Specification of test tubes.

tube	G-1	H-1	H-2	H-3	H-4	H-5	H-6
d_i [mm]	6.36	6.40	6.32	6.33	6.34	6.31	6.32
h [mm]	0.21	0.22	0.18	0.16	0.17	0.20	0.14
β [°]	18	16	14	14	8	28	8
n [-]	50	58	59	58	62	50	61
η	1.81	2.15	1.83	1.74	1.93	2.02	1.78

d_o = 7.00 mm

(a) droplet flow ratio F_d (b) circulation flows in cross section

Fig. 8 Droplet and flow field in tube cross secction.

4. CORRELATION OF PRESSURE LOSS

4.1 Friction factor of single phase flow in microfin tubes

Although the pressure loss in heat exchanger mainly occurs during condensation and evaporation two phase flows, single phase flow, which are subcooled liquid and super heated vapor, could not be neglected and prediction of the pressure loss is required. More important roles of the prediction of single phase pressure loss are to predict the two phase flow pressure loss and heat transfer coefficient. According to the Martinelli's method, the two phase pressure loss can be calculated by multiplying two phase flow multiplier to single phase pressure loss. Therefore, accuracy of the prediction of single phase pressure loss directly affects on the calculation of two phase pressure loss. The friction factor of single phase flow also appears in correlation of heat transfer coefficient, as explained later.

There are some correlations proposed for helical microfin tubes and a few for herringbone microfin tubes. Although the correlations could be predict their own data and some other data from literature, there are limitations and relatively large errors to predict other data with different fin shape and refrigerant. For example, although Wang et al.[10] reported that Jensen-Vlakancic correlation predicts well their database, Goto et al. mentioned that Jensen-Vlakancic correlation shows under predict their data. Therefore more reliable correlation is desired. Many of the correlations are empirically obtained and many of them are the type of $f=CRe^n$ and the factor C and exponent n are determined to fit the each experimental data. We have proposed a correlation through a semi-analytical approach using the wall law for herringbone microfin tubes [16] and helical microfin tubes [17], where equation type of the correlation was derived from an analytical method and parameters fitted by wide range experimental data. The proposed correlations, which are shown below, have been compared with data obtained by other researchers to confirm the reliability. Details of derivation is explained elsewhere [16,17].

Helical :
$$\frac{1}{\sqrt{f}} = -4.5 - 4.0\log_{10}\left(\alpha\,\frac{h}{d_i} + \frac{0.1414}{\mathrm{Re}\sqrt{f}}\right), \quad \alpha = \eta^{3.7}\left[0.0019\left\{1 - 0.92(\cos\beta)^{3.8}\right\}\right] \quad (1)$$

Herringbone:
$$\frac{1}{\sqrt{f}} = -5.0 - 4.0\log_{10}\left(\alpha\,\frac{h}{d_i} + \frac{0.1414}{\mathrm{Re}\sqrt{f}}\right), \quad \alpha = \eta^{2.33}\left[0.0115\left\{1 - 0.98(\cos\beta)^{4.7}\right\}\right] \quad (2)$$

Fig. 9 shows relations of friction factors versus Reynolds number for the helical (white symbols) and herringbone (black symbols) tubes. The data scattered over wide range in dependence on the fin geometry. Comparison between experimental friction factor and correlation is shown in Fig.10. Fin geometries are shown in Table 1 for herringbone microfin tubes and Table 2 for helical microfin tubes. As shown in the figures, good agreement is obtained.
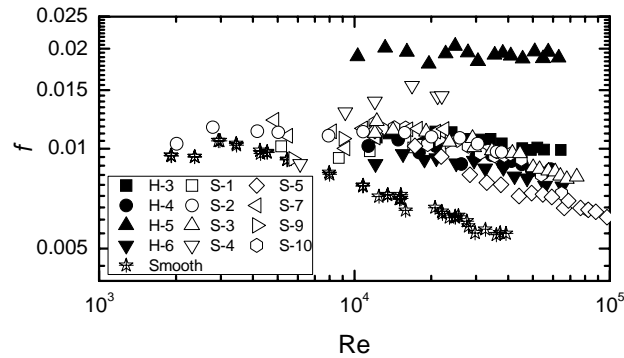

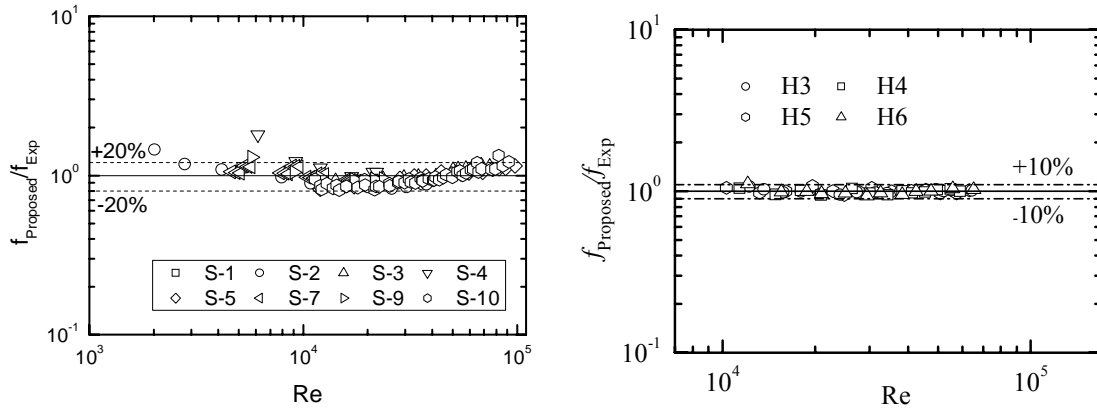**Fig. 9 Friction factors of helical and herringbone micorfin tubes.**

Fig. 10 Comparison between experimental friction factor and correlation.

Table 2 Specification of helical microfin tubes.

tube	S-1	S-2	S-3	S-4	S-5	S-6	S-7	S-8	S-9	S-10
d_i [mm]	6.32	6.36	6.35	6.35	6.41	6.30	6.25	6.26	6.27	6.36
h [mm]	0.16	0.21	0.19	0.22	0.19	0.22	0.22	0.22	0.20	0.21
β [°]	18	9	18	30	18	18	10	17	7	18
n [-]	60	60	60	60	30	50	70	70	85	50
η	1.70	2.06	2.00	2.27	1.53	1.90	2.32	2.34	2.46	1.83

$d_o = 7.00$ mm

4.2 Frictional pressure loss of two phase flow in microfin tubes

Two phase flow multiplier is a function which is mainly dominated by Lockhart-Martinelli parameter X_{tt} and many correlations of the two phase flow multiplier ϕ_v have been proposed as a function of Lockhart-Martinelli parameter X_{tt}.

$$X_{tt} = \left(\frac{1-x}{x}\right)^{0.9}\left(\frac{\rho_v}{\rho_l}\right)^{0.5}\left(\frac{\mu_l}{\mu_v}\right)^{0.1} \tag{3}$$

Because the relation between the multiplier and X_{tt} varied for mass velocity condition and tube diameter, modified correlations have also proposed. We were obtained a correlation by referring the previous studies and following preliminary correlation was derived.

$$\phi_v^2 = 1 + CX_{tt}^n + X_{tt}^2 \tag{4}$$

$$C = 21\left\{1 - \exp\left(-0.28Bo^{0.5}\right)\right\}\left\{1 - 0.9\exp\left(-0.05Fr^{1.1}\right)\right\}, \quad n = Bo\left\{1 - 0.992\exp\left(-0.0007Fr\right)\right\}$$

$$Bo = gd_i^2(\rho_l - \rho_v)/\sigma \ , \quad Fr = G/\sqrt{\rho_v(\rho_l - \rho_v)gd_i^2}$$

As shown in Fig. 10, the two phase flow multipliers ϕ_v are well correlated with above equation and the predicted pressure droop agree with experimental data.
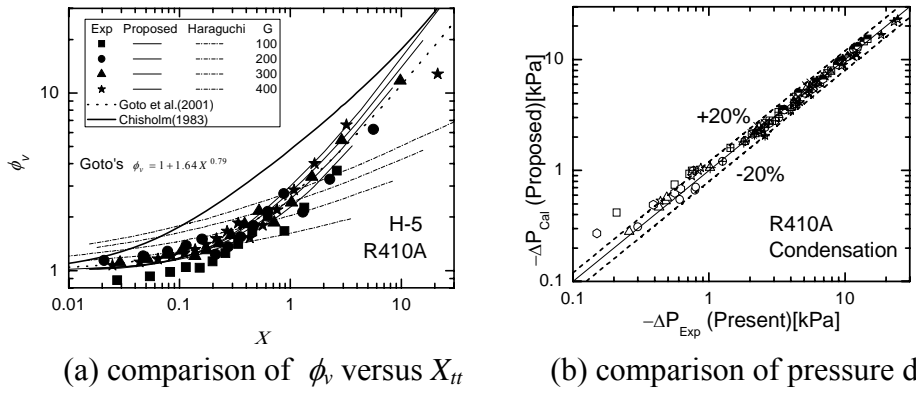

(a) comparison of ϕ_v versus X_{tt} (b) comparison of pressure drop

Fig. 10 Comparison between experimental friction factor and correlation.

5. CORRELATIONS OF HEAT TRANSFER COEFFICIENT

5.2 Condensation

Correlations of condensation heat transfer coefficient in microfin tubes have been proposed by many researchers. Here, newly proposed correlation [14] is introduced. It is noted that the heat transfer coefficient α_η is defined with actual area (= $\eta \times$area of equivalent smooth tube). As mentioned above, fiction factor of vapor f_v is used in the correlation.

$$Nu = \frac{\alpha_\eta d_i}{\lambda_l} = \left(Nu_F{}^2 + Nu_B{}^2\right)^{1/2} \tag{5}$$

$$Nu_F = 2.12\sqrt{f_v}\phi_v\left(\frac{\rho_l}{\rho_v}\right)^{0.1}\left(\frac{x}{1-x}\right)Re_l^{0.5}\,Pr_l^{0.5} \ , \quad Nu_B = 1.98\frac{H(\xi)}{\eta^{0.5}Bo^{0.1}}\left(\frac{GaPr_l}{Ph}\right)^{1/4}$$

$$H(\xi) = \xi + \left[10(1-\xi)^{0.1} - 8.9\right]\sqrt{\xi}\left(1 - \sqrt{\xi}\right), \quad \xi = 0.81\xi_{Smith} + 0.19x^{100(\rho_v/\rho_l)^{0.8}}\xi_{Homo}$$

$$\xi_{Smith} = \left[1 + \frac{\rho_v}{\rho_l}\left(\frac{1-x}{x}\right)\left(0.4 + 0.6\sqrt{\frac{\rho_l/\rho_v + 0.4(1-x)/x}{1 + 0.4(1-x)/x}}\right)\right]^{-1} , \quad \xi_{Homo} = x\left[x + (1-x)\frac{\rho_v}{\rho_l}\right]^{-1}$$

$$Bo = \frac{(p-t)d_i g(\rho_v - \rho_l)}{\sigma}$$

5.2 Evaporation

There are some correlations to predict heat transfer coefficient of evaporation in helical microfin tubes. Here, a new correlation proposed by Mori et al. [15] is introduced. They separate the heat transfer coefficient α into bottom part α_B where liquid covers microfins and top part α_T where meniscus liquid is formed in the grooves. The heat transfer coefficients and angle φ_S which indicates the separation point are calculated from following equations.

$$\alpha = \frac{\varphi_S}{\pi}\alpha_B + \left(1 - \frac{\varphi_S}{\pi}\right)\alpha_T \tag{6}$$

$$\alpha_B = \left[1 + C_f X_{tt}^{-0.93} + C_b\left(Bo \times 10^4\right)^{0.8}\right]\alpha_l \ , \quad \alpha_l = \frac{\lambda_l}{d_i}0.023\eta^{1.3}\left[\frac{G(1-x)d_i}{\mu_l}\right]Pr_l^{0.4}$$

$$\frac{\varphi_S}{\varphi_0} = 1 + 0.75\left[\frac{x}{1-x}\left(\frac{\rho_l}{\rho_v}\right)^{0.5}\right]^n \exp\left[1.06 - 23.8\left(\frac{\rho_v}{\rho_l}\right)\right]$$

$$n = 0.26\left[\frac{G^2}{gd_i\rho_v(\rho_l - \rho_v)}\right]^{0.42}\left(\frac{q}{G\Delta h_v}\right)^{-0.16} \ , \quad \left[1 + \frac{1-x}{x}\left(\frac{\rho_v}{\rho_l}\right)\right]^{-1} = 1 - \frac{\varphi_0 - \sin\varphi_0\cos\varphi_0}{\pi}$$

$$Bo = \frac{q}{G\Delta h_v} \ , \quad X_{tt} = \left(\frac{1-x}{x}\right)^{0.9}\left(\frac{\rho_v}{\rho_l}\right)^{0.5}\left(\frac{\mu_l}{\mu_v}\right)^{0.1} \ , \quad C_b = \left[1.6 + \left(\frac{1}{X_{tt}}\right)^{0.3}\left(\frac{Gd_i}{\mu_l}\times 10^{-4}\right)^{0.3}\right]^{-1}$$

$$C_f = 37\left(\frac{h}{d_i}\right)^{-0.4}\left(\frac{t}{d_i}\right)^{0.8}\left(\frac{Gd_i}{\mu_l}\times 10^{-4}\right)^{-0.65}\left[1 - 0.93\exp\left(-5\frac{Gd_i}{\mu_l}\times 10^{-4}\right)\right]\left(\frac{\rho_v}{\rho_l}\right)^{0.45}$$

$$\alpha_T = C_m\frac{\lambda_l}{t}$$

$$C_m = 530\left(\frac{h}{d_i}\right)^{0.8}\left(\frac{G^2 t}{\sigma\rho_l}\right)^{0.15}\left[1 - 0.6\left(1 + 25\left(\frac{G^2 t}{\sigma\rho_l}\right)^{1.2}\left(Bo\times 10^4\right)^{0.5}\right)^{-1}\right]\left(\frac{1}{X_{tt}}\right)^{0.2}$$

6. CONCLUSIONS AND FUTURE RESEARCH

Ozone layer depletion and global warming demand big changes of air conditioners, heat pumps, and refrigeration systems. Refrigerants used in these systems have to move from hydro-fluorocarbons to natural refrigerants or chemical compounds with zero ozone depletion potential and low global warming potential. Energy consumption should be also reduced as much as possible. In order to solve these problems, developments of new heat exchangers suitable for new refrigerants are required. Although the microfin tubes have worked well on the fluorocarbons, it has not been clarified that they are available to new refrigerants. In the case of high pressure refrigerants, tube diameter would be smaller than those of conventional ones. Small diameter tubes might be required for high-performance compact heat exchangers. For the small channel, optimum fin shape would be different. Additionally, when the small tubes are used, refrigerant is separated into multi path and uniform distribution is needed.

NOMENCLATURE

di	mean diameter [m]		x	quality
G	mass velocity [kg/(m^2·s)]		α	heat transfer coefficient [kW/(m^2·K)]
g	Gravitational acceleration [m/s^2]		η	area augmentation ratio
Δh_v	heat of absorption [kJ/kg]		λ	thermal conductivity [W/(mK)]
q	heat flux [kW/m^2]		μ	viscosity [Pa.s]
Re	Reynolds number		ρ	density [kg/m^3]
t	with of top opening of grooves [m]		σ	surface tension [N/m]

REFERENCES

1. K. Fujii, N. Itoh, T. Innami, H. Kimura, N. Nakayama, and T. Yanugidi, Heat Transfer Pipe, U.S. Patent 4,044,797, assigned to Hitachi, Ltd.
2. M. Itoh, From my Experience in Development of Heat-transfer-improved Tubes, J. HTSJ, 42(174) (2003) 32.
3. T. Fuii, S. Koyama, N. Inoue, K. Kuwahara, S. Hirakuni, An experimental study of evaporation heat transfer of refrigerant HCFC22 inside an interenally grooved horizontal tube, Trans. JSME, 59(652) (1993) 2035.
4. S. Nozu, H. Honda, Condensation of refrigerants in horizontal, spirally grooved microfin tubes: Numerical analysis of heat transfer in the annular flow regime, Trans. ASME, J. Heat Transfer, 122 (2000) 80-91.
5. S. Yoshida, H. Mori, Heat transfer in evaporator tube, Refrigeration, 75(874) (2000) 649-653.
6. S. Nozu, H. Katayama, H. Nakata, H. Honda, Condensation of a refrigerant CFC11 in horizontal microfin tubes (Proposal of correlation equation for frictional pressure gradient), Exp. Thermal & Fluid Science, 18 (1998) 82-96.
7. M.A. Islam, A. Miyara, Liquid film and droplet flow behaviour and heat transfer characteristics of herringone microfin tubes, Int. J. Refrigeration, 30 (2007) 1408-1416.
8. A. Miyara, Y. Otsubo, S. Ohtsuka, Effect of fin shape on condensation heat transfer and pressure drop inside herringbone micro fin tubes, Trans. JSRAE, 18(4) (2001) 463-472.
9. A. Miyara, Y. Otsubo, S. Ohtsuka, Evaporation heat transfer of R410A in herringbone micro fin tubes, Proc. IIR Conf. B1, Thermophysical Properties and Transfer Processes, (2001) B2.9-B2.14.
10. H.S.Wang, J.W.Rose, Prediction of effective friction factors for single-phase flow in horizontal microfin tubes, 27 (2004) 904-913.
11. N. Inoue, M. Goto, Development of general correlations for pressure drop in single-phase turbulent flow inside internally helically grooved tubes, Proc. The 3rd Asian Conf. Refrig. and Air-cond., (2006) 521-524
12. H.M.M. Afroz, A. Miyara, Friction factor correlation and pressure loss of single-phase flow inside herringbone microfin tubes, Int. J. Refrigeration, 30(7) (2007) 1187-1194.
13. H.M.M. Afroz, A. Miyara, A new correlation of single-phase friction factor for helical microfin tubes, Proc. 4th BAME-ASME Int. Conf. Thermal Eng. (2008).
14. R. Yonemoto, S. Koyama, Experimental study on condensation of pure refrigerants in horizontal micro-fin tubes –proposal of correlation for heat transfer coefficient and frictional pressure drop–, Trans. JSRAE, 24(2) (2007) 139-148.
15. H. Mori, S. Yoshida, S. Koyama, A. Miyara, S. Momoki, Prediction of heat transfer coefficient flowing in horizontal, spirally grooved evaporator tubes, Proc. 2002 JSRAE Conf. (2002) 547-550.

"SEEING" CRACKS IN STRUCTURAL MATERIALS USING THERMAL IMAGING TECHNIQUES

Golam M. NEWAZ

Department of Mechanical Engg.
Wayne State University
5050 Anthony Wayne Drive
Detroit, Michigan 48201, USA
e-mail: gnewaz@eng.wayne.edu

ABSTRACT

Two thermal techniques are discussed which allow detection of damage and cracks in structural materials. The first technique is known as "thermal wave imaging" where temperature decay is monitored on the surface after flash lamp heating and since thermal diffusivity and conductivity are altered locally due to internal damage, temperature distribution profile on material surface provides information about damage. Another technique, "Sonic IR" which employs ultrasonic excitation of cracks generating heat due to friction of mating crack surfaces which can also be used to detect cracks in structural materials and other types of damage such as delamination in composites. It is shown that a dynamic finite-element model can reproduce the experimentally observed occurrence of acoustic chaos from a single-frequency input. The resulting sound spectrum consists of fractional "infra harmonics" and very many harmonics of the fundamental infra harmonic. These dense spectra are essential for reliable crack detection in Sonic IR imaging.

KEY WORDS. Thermal wave imaging, ultrasonic excitation, infrared, cracks and damage, delamination, composite.

1. INTRODUCTION

1. 1 Thermal Wave Imaging

In a Pulse–echo Thermal Wave IR Image System, a pulse of heat is launched to specimens by flash lamps and the thermal signal amplitude distribution of the specimen is monitored as a function of time by an infrared camera (Fig. 1).
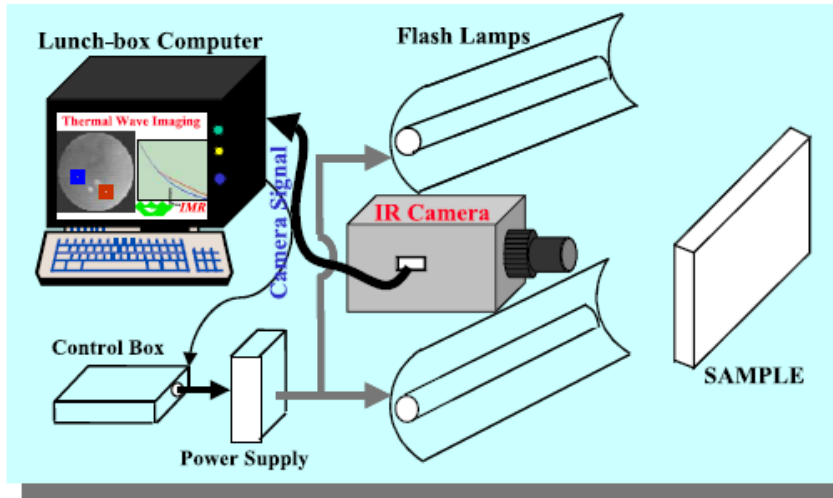
Fig. 1 A thermal wave imaging system.

The thermal signal amplitude of specimens increases very steeply during the exciting pulse. Then, the deposited energy diffuses progressively into the specimen by conduction. The temperature field T in the specimen after exited pulse is given by [6]

$$T(x,t) = \frac{Q}{\rho c (4\pi\alpha t)^{1/2}} e^{-\frac{x^2}{4\alpha t}} \qquad\qquad t > 0 \qquad\qquad (1)$$

where Q is the amount of heat exited by pulse; c, ρ and α are the specific heat capacity, the density and thermal diffusivity of the material, respectively; t is the time after flashing; and x is the depth in the sample. When x = 0, T(t) represents thermal signal amplitude.

Thermal wave imaging (TWI) technique for nondestructive testing of materials is based on the fact that a defect region generally has a thermal conductivity difference from that of the reference region in the sample. Therefore, heat flows differently through the defect region than through the reference region. Differences in the heat flow result in differences in temperature distribution on the surface of the sample. Zones with defects have trapped air. Surface temperature above the defect is hotter and it decays more slowly. A temperature distribution map can show hot spots and also elevated thermal wave amplitude signals.

1.2 Sonic IR Imaging

Frictional heating generated by low-frequency ultrasound makes cracks in solids visible to infrared (IR) cameras. These effects are caused by the fact that the two surfaces of internal defects do not move in unison when sound propagates in the object. The resultant frictional heating provides the IR radiation that is detected by the camera. In the version of this technology practiced by the authors, the acoustic excitation is applied in the form of short (typically, 50–500 ms) pulses whose nominal frequency is either 20kHz or 40kHz. Both surface-breaking and subsurface cracks can be detected by this method, but images of subsurface cracks are blurred by lateral heat diffusion before a significant

heating of the object's surface occurs. When using laser vibrometers to study vibration patterns in samples, we discovered that when the best images were obtained, the acoustic vibration was NOT a single frequency vibration, but rather had a complicated waveform, the details of which often switched during the course of the excitation pulse. We have dubbed this complicated acoustic behavior "acoustic chaos" [2].

2. EXPERIMENTAL ASPECTS

2.1 Example of Thermal Wave Imaging

Thermal barrier coated (TBC) Nickel based Rene N5 superalloy samples (25.4 mm dia and coating thickness of 3.2 mm) were thermally cycled between 200-1177C and were monitored for internal delaminations between the coating and the superalloy substrate. The TBC is partially stabilized zirconia – a ceramic material. Initial growth of delamination was observed after 2 cycles as shown in Figure 2. Thermal wave signal from delaminated and undelamianted regions show that the temperature decay on the coating above the whitish delamination is slower.
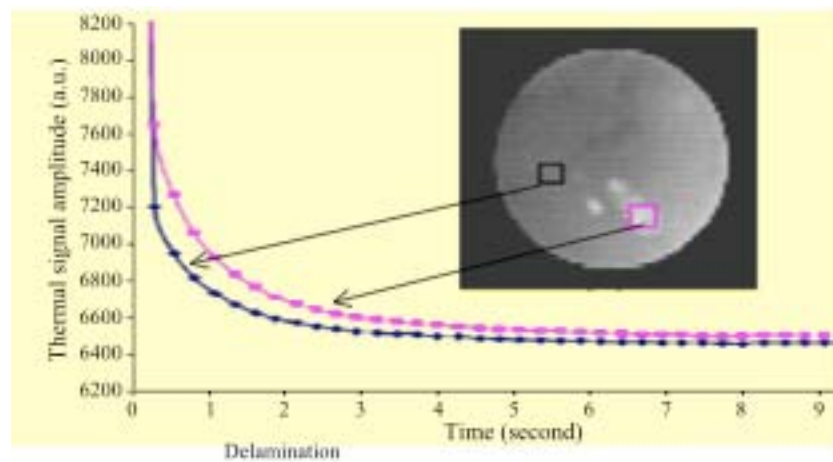

Fig. 2 Slower heat diffusion (whitish regions) in delaminated areas in TBC sample.

2.2 Example of Sonic IR Imaging

We have demonstrated experimentally that there exist cracks that are extremely difficult, or even impossible to detect using conventional fixed-frequency Sonic IR, but are readily detected when the excitation is chaotic. In Fig. 3 we show the advantage of chaotic sound excitation for experimental application to crack detection in metallic structures. Fig. 3a shows a Sonic IR image of a small fatigue crack in the surface of a nickel alloy bar. This image was made using an 800 ms pulse of chaotic sound that was generated by a transducer/acoustic horn combination that nominally produces 40 kHz ultrasound, but which here was configured to produce chaotic sound. Fig. 3b shows the same bar, but with the source configured to inject an 800 ms pulse of pure 40 kHz ultrasound of the same power as in Fig. 3a.
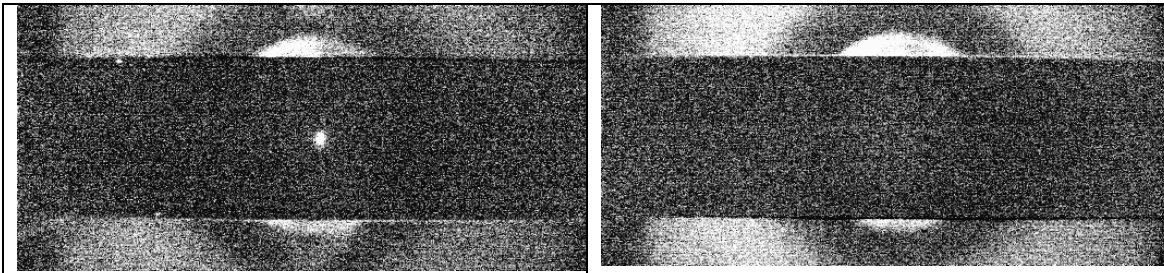
Fig. 3a. A Sonic IR image of a fatigue crack in the center of a nickel alloy test bar made using an 800 ms long pulse of *chaotic* sound originating from a transducer that nominally produces 40 kHz ultrasound. The bar is about 3 cm high and 1.3 cm thick. The crack is the small bright spot in the center of the bar. The bright circular object behind the bar is the ultrasonic horn used to inject the sound.	**Fig. 3b. A Sonic IR image of the the same nickel alloy test bar made using an 800 ms long pulse of *non-chaotic* 40 kHz ultrasound originating from the same transducer as in Fig. 3a. The ultrasonic power was the same as that used in Fig. 3a, but the crack is *not* visible. The background is brighter here because the AGC was attempting to find contrast in a ROI at the center of the bar where there is none.**

Chaotic effects, including the appearance of fractional frequencies result from the non-linear interaction between the ultrasonic source and the sample. These unexpected frequencies are the major source of crack heating in Sonic IR imaging. Enhanced crack heating results from the dense acoustic spectrum produced by 'infra-harmonics' and their corresponding harmonics.   As demonstrated in Figure 3, single frequencies are much less effective in crack heating, and consequently less useful for IR crack detection. The transducer-sample interaction has been modeled using a vibrating mass bouncing against a rigid wall with a constant applied force [3]. In this analytic model, the mass vibrates sinusoidally with a fixed frequency. This model produces the characteristic infra-harmonic behavior, with frequent switching of the fractional infra-harmonic fraction during short intervals of pure chaos. Dynamic finite-element models [4] have confirmed the analytic results, and both are in good agreement with experimental results. In Figure 4, we show both an experimental spectrum and a theoretical spectrum obtained from a finite element model designed to simulate the experiment as closely as possible. The similarity between the two spectra is not perfect, but it is clear that the same phenomenon is occurring in both the experimental and model results. The origin of this phenomenon is in the non-linearity resulting from the "bouncing" of the transducer on the surface of the sample.

4. CONCLUSIONS

Thermal wave imaging and Sonic IR are effective damage and crack detection techniques for structural materials. Examples are shown to demonstrate their efficacy. For sonic IR, acoustic chaos increases the efficiency of crack detection in Sonic IR imaging. This phenomenon can be understood in terms of both analytic and finite-element models, and is the result of the bouncing of the transducer on the sample's surface. The model results and experiments are in quite close agreement for a model of a chaotic non-linear phenomenon. Sonic IR is an extremely fast technique.
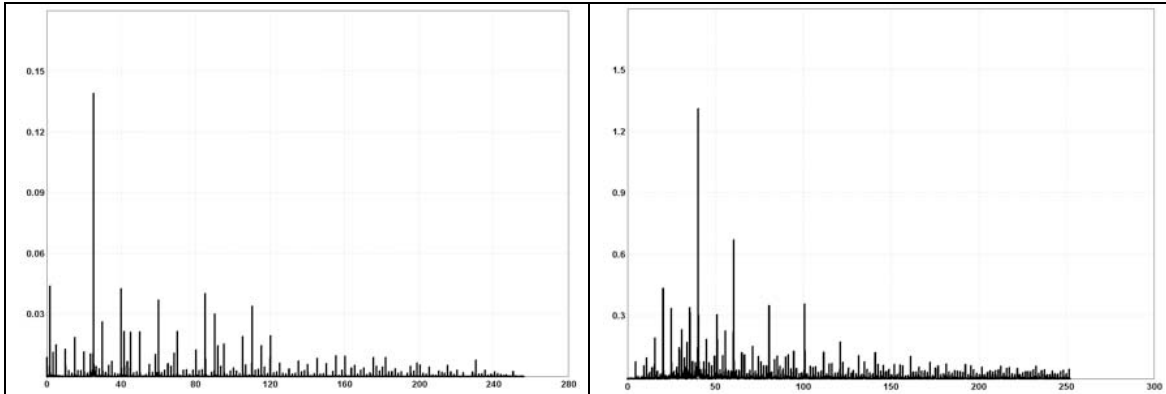
Fig. 4a. An experimental spectrum of chaotic sound in a test bar. The lowest frequency in this spectrum is about 1.66 kHz, or 1/12 of the 19.88 kHz driving frequency of the ultrasonic horn. The remaining frequencies are all integral multiples of this "fundamental" frequency. It is interesting to note that the largest peak in the spectrum is not at the driving frequency, but at 24.8 kHz, or 15/12 of the horn's frequency.	Fig. 4b. A spectrum of chaotic sound in a test bar calculated from a dynamic finite-element model. The lowest frequency in this spectrum is about 1.54 kHz, or 1/13 of the 20.0 kHz driving frequency of the ultrasonic horn. The remaining frequencies are all integral multiples of this "fundamental" frequency. The largest peak in this spectrum is the 40kHz harmonic of the 20kHz driving frequency.

5. NOMENCLATURE

α thermal diffusivity   c specific heat capacity
ρ density   Q heat from thermal pulse

6. REFERENCES

[1] A.V. Luikov, Analytical Heat Diffusion Theory, Academic Press, New York, 1968, pp. 381.
[2] Xiaoyan Han, Zhi Zeng, Wei Li, Mahmad Islam, Jianping Lu, Vera Loggins,and L.D. Favro, G.M. Newaz, and R.L. Thomas: Acoustic Chaos for Enhanced Detectability of Cracks by Sonic Infrared Imaging, J. Appl. Phys. 95, 3792-3797, 2004
[3] Xiaoyan Han, V. Loggins, and Zhi Zeng, L.D. Favro, R.L. Thomas, Mechanical Model for the Generation of Acoustic Chaos in Sonic IR Imaging: Applied Physics Letters, 85, No.8, pp1332-1334, 2004
[4] Xiaoyan Han, Md. Sarwar Islam, G. Newaz, L.D. Favro, R.L. Thomas, Finite-Element Modeling of Acoustic Chaos by Sonic Infrared Imaging: J. Appl. Phys. 98, 1, 014907, 2005

ADVANCES IN NANOSCALE REINFORCEMENT OF TEXTILE POLYMERS

Hassan Mahfuz [1], Mujibur R. Khan [1], Ashfaq Adnan [2], Mohammad M. Hasan [3], Vijaya K. Rangari [4], Vinod Dhanak [5] and Shaik Jeelani [4]

[1]*Department of Ocean Engineering, Florida Atlantic University, Boca Raton, FL33431, USA*
hmahfzu@fau.edu
[2] *Department of Mechanical Engineering, Northwestern University, Evanston, IL 60208, USA*
[3]*Department of Mechanical and Industrial Engineering, University of Toronto, Ontario, Canada M5S 3G8*
[4]*Tuskegee University's Center for Advanced Materials (T-CAM), Tuskegee, AL 36088*
[5]*Physics Department, University of Liverpool, and Daresbury Laboratory, Warrington, WA4 4AD, UK*

ABSTRACT

Textile polymers such as polyethylene and nylon have been used for many years to extract useful fibers. As with many other polymers there have been continuing efforts to enhance strength, stiffness and fracture toughness through nano- or micro-scale inclusions. In recent years it has been convincingly shown that nanoscale inclusions have distinct advantage of creating large interface with the polymer and hence influence the mechanical properties more rigorously. Attempts have been made to increase strength and modulus of linear low density polyethylene (LLDPE), nylon-6, and low density polyethylene (LDPE) using nanoscale inclusions such as carbon nanoparticles, carbon nanotubes (CNTs), and silica nanoparticles. In some cases, silica nanoparticles and CNTs were functionalized to control the ultimate fracture strain. Polymers were dry mixed with the nanoscale inclusion and melt extruded into filaments. Loading of particles remained within 1-4 wt% of the polymer. Melt extrusion was followed by stretching to ensure further alignment of particles along the filament length. Once stabilized, filaments were tested either in fiber or consolidated form. Thermal and mechanical tests have revealed that there are significant improvements in thermal decomposition temperature, strength, and stiffness of the nanocomposites due to nanoscale reinforcement. An overview of various reinforcements and their influence on polymer properties are described in the paper.

1. INTRODUCTION

It has been established in recent years that polymer based composites reinforced with a small percentages of strong fillers can significantly improve the mechanical, thermal and barrier properties of the pure polymer matrix [1–6]. Moreover, these improvements are achieved through conventional processing techniques without any detrimental effects on processability, appearance, density and ageing performance of the matrix. Eventually, these composites are now being considered for a wide range of applications including packaging, coating, electronic, automotive and aerospace industries.

When enhancements in mechanical properties are of major concern, it is well known that the load transfer mechanisms between the filler particle and the matrix at their interfaces become important. The strength and stiffness of the material is directly related to the characteristics of these interfaces. When these fillers are rod-shaped, the surface area per particle will be higher than any other shape of fillers, and thereby contribute more in the load transfer. As a result, the scope of research on aligned rod-shaped fillers is increasing day by day. Recently, vapor grown

1

carbon fibers (VGCF) was introduced with much smaller dimensions than traditional fillers [7, 8]. As these types of fibers have attractive aspect ratios, several researchers attempted to develop suitable techniques to align discontinuous fibers along preferred directions within the composite materials [9-11]. Among several other fiber aligning techniques, 'Extrusion' has been found to be one of the most widely used fiber-aligning methods [12-15]. However, the term 'Extrusion' indicates a kind of process, which involves some factors that should be carefully considered in order to establish a successful fiber or particle aligning technique. The starting materials and their chemical compositions, their mixing techniques, type of extruder, material loading process, and extrusion temperature etc. play significant roles which can eventually alter the characteristics of the end products. Considering the properties of vapor grown carbon fibers as mentioned earlier, it seems that they can be used for fiber alignment using extrusion. However, the major problem associated with VGCF is that they become highly agglomerated, randomly aligned and entangled during production. Therefore, it does not seem to be viable that VGCF can be used in a single screw extrusion machine. But there is a good possibility that if these entanglement or agglomeration can be reduced in the production phase, the use of single screw extrusion might be possible. One such method of producing carbon nanoparticles/whiskers with minimal agglomeration is Catalytic Vapor Deposition (CCVD) process.

In order to utilize the extraordinary strength and stiffness of carbon nanotubes, usually in the range of 200-900 MPa and 200-1000 GPa, respectively in bulk materials, several researchers have attempted to align CNTs along preferred directions [16-21]. Almost all of these attempts were made with the infusion of single or multiwalled CNTs, or vapor grown carbon nanofibers (CNF) into thermoplastic polymers. Infusion was carried out either through a liquid route using sonication, or a dry route followed by melt mixing in an extruder. Alignment of CNTs or CNFs in the composite was enforced by extrusion or spinning and accompanied by subsequent stretching. The resulting composites either in consolidated or filament form have no doubt demonstrated improved mechanical and thermal properties.

Nylon's toughness, low coefficient of friction and good abrasion resistance make it an ideal replacement for a wide variety of applications replacing metal and rubber. The amide groups of nylon are very polar, and can hydrogen bond with each other. Because of these, and because the nylon backbone is so regular and symmetrical, nylons are partially crystalline, and they make very good fiber [22-26]. Nylons are made from a monomer, such as a cyclic amide called lactam. For example, Caprolactam is a lactam with six carbon atoms and nylon made from Caprolactam is called nylon 6. When nylon is spun into fibers, the long chain-like macromolecules line up parallel to each other. The amide groups on adjacent chains then form strong bonds with each other called hydrogen bonds. These hydrogen bonds hold the adjacent chains together, making nylon yarn strong. When nylon-6 polymerizes, the amide link present in Caprolactam (starting monomer for nylon-6) opens up and the molecules join up in a continuous chain providing an ideal mechanism for interacting with nanoparticles. On the other hand, silica particles are formed by strong covalent bonds between silicon and oxygen atoms by sharing their electron pairs at the p orbitals. In addition, the surface bound OH groups on silica surfaces offer an opportunity to form stable bonds with nylon or any functional group during polymerization.

Polyethylene (PE) is a polymer based only on carbon and hydrogen, originating from monomers containing a double bond. The generic chemical formula for polyethylene is - $(C_2H_4)_n$- where n is the degree of polymerization. The density of the polyethylene decreases with increased side group mole fraction. These polyethylene's generally have branched and linear chain structures each with a molecular weight of typically less than 50,000 g/mol.[1,2] Low density polyethylene is considered as one of the commercially important thermoplastics, especially for their low density, good processability, and easier mouldability for a wide range of applications . LDPE is more flexible than HDPE, which makes it a good choice for prosthetic devices.

On the other hand Ultra high molecular weight polyethylene (UHMWPE) is a linear homopolymer with average molecular weight of 3-6million g/mole. For UHMWPE, the

molecular chain can consists of as many as 200000 ethylene repeat units. Despite the relatively weak Van der Waals bonds between its molecules, the longer chain serves to transfer load more effectively to the polymer backbone by strengthening intermolecular interactions. This results in a very tough material, with high impact strength. At molecular level the carbon backbone can twist, rotate and fold into ordered crystalline regions. The molecular chain of UHMWPE is a long tangled string of spaghetti. As the chain is imbued with internal energy the molecular chain can become mobile at elevated temperatures. Upon cooling below the melting temperature the molecular chain have the affinity to rotate to create chain folds [27-28].

In the last few years systematic advances have been made to use this nanoparticle inclusion technology into various thermoplastic polymers to enhance both mechanical and thermal properties. Description of each of the systems ensues.

2. FILAMENT EXTRUSION

Nanoparticles (pristine/ functionalized) were dry mixed with the polymer in powder form. The amount of nanoparticles loading varied from 1 to 4 wt%. The dry-mixed powder was then melted in a single screw extruder which was followed by distributive mixing, extrusion, stretching, and heat stabilization to continuously draw nanoparticle-reinforced filaments. In parallel, control filaments were also extruded using identical procedures. The dry mixing of polymer powder with nanoparticle was performed in a mechanical blender for three hours. In order to eliminate moisture the mixture was placed into a drying chamber. Hot air was supplied to the chamber through an insulated flexible tube using a vortex blower. Prolonged heating accompanied with a vortex flow broke up large agglomerates of nanoparticles if any left after the mechanical blending. Once the mixture was ready, it was extruded through a *Wayne Yellow Label Table Top Extruder.* Five thermostatically controlled heating zones were used to melt the admixture prior to extrusion. The die zone consisted of a circular plate, 10 cm long steel tubing with an inner diameter of 4 mm, and the die itself. A distributive mixing of the nanoparticles with polymer was enforced through the use of a circular plate with multiple orifices. A specially designed die was used in the process. The die configuration generated two distinct flow regimes that significantly affected the distribution of the particles. After extrusion, filaments were solidified by passing them through chilled water maintained at approximately 10^0C. In the next step, filaments were stretched using a tension-adjuster (Godet), and heat stabilized unit. The heater temperature, and the filament travel per minute (FPM) was adjusted in the Godet stations to allow continuous drawing of filaments. Finally, the filaments were wound on a spool using a filament winder at a winding speed of about 70 rpm.

3. RSULTS AND DISCUSSIONS

The neat and nanophased samples were examined using *Phillips-201,* Transmission Electron Microscopy (TEM), Field emission scanning electron microscope (FE-SEM, Hitachi S-900). *Rigaku D/MAX 2200* X-Ray Diffractometer, TA Q1000 Differential scanning calorimeter, Fourier Transform Infrared (FTIR) Spectroscopy and Zwick/Roell Z050 tensile testing machine with 20 N load cell. The following is a description of a series of experiments that were performed with various polymers reinforced with a variety of nanoscale reinforcements.

3.1 Linear low density polyethylene (LLDPE) reinforced with carbon nanoparticles and whiskers [29]

The failure stress of the extruded polyethylene sample doped with carbon nanoparticles/whiskers is about 17% higher than the neat extruded sample. The gain in tensile strength and modulus is 16.9% and 16% respectively. The gain in modulus is at the cost of a
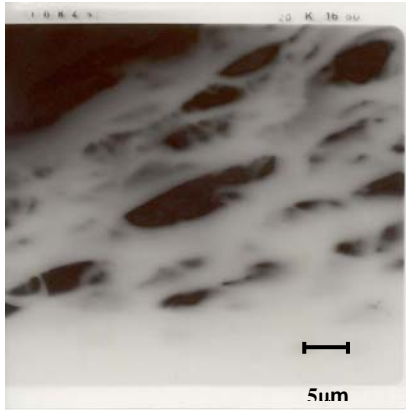
3

Fig 1: *TEM micrograph of carbon nanoparticles/whiskers reinforced polyethylene*

reduction in failure strain to about 12%. Enhancement in strength by about 15-16% was somewhat surprising since that was not the usual case with vapor grown fibers. Usually, enhancement up to this scale was obtained only when significant percentage (about 5-10% by weight) of fillers were added. To investigate the degree of alignment, Transmission Electron Microscopy (TEM) studies were conducted as shown in Fig 1. The black spots represent the embedded nanoparticles/whiskers in the polyethylene matrix. The picture clearly shows that the carbon whiskers are aligned in a unidirectional manner along the length of the filament. The reduction in ultimate strain, and increase in stiffness are mainly due to better interfacial bonding between the whiskers and the surrounding polymer, and enhanced cross-linking in the matrix, which was caused by the presence of nanoparticles, shearing at high temperature, and subsequent stretching during fabrication.

3.2 LLDPE infused with Carbon nanotubes (CNTs) [30]

The crystalline nature of fabricated and as-received materials has been characterized by X-ray diffraction (XRD) as shown in Fig 2. The half width of the 110 reflection of the nanocomposite (0.4^o) is almost half of the neat polyethylene (0.8^o). The half width values clearly indicate that the nanocomposite materials are more crystalline than the neat polyethylene. The addition of CNTs to the polymer provides a large interface between the CNTs and polymer which in turn creates very suitable conditions for the nucleation and crystallization process that takes place during heating [31,32]. In addition, the presence of CNTs restricts the entanglement of polymer chains to a lesser extent and allows some degree of orderly orientation during polymerization giving rise to increased crystallinity. DSC tests of neat-polyethylene, and CNT-polyethylene suggests that the melting endotherm is higher in case of CNT-polyethylene. The crystallinity of neat and CNT-polyethylene is 12% and 29%, respectively. It is also
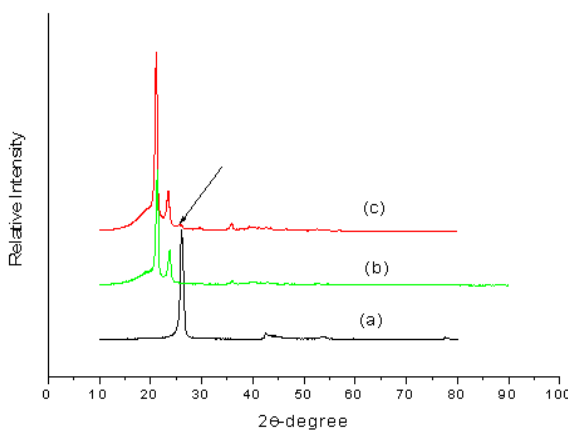

Fig 2: *X-ray diffraction of: a) neat CNT b) neat polyethylene. c) CNT-polyethylene nanocomposite*
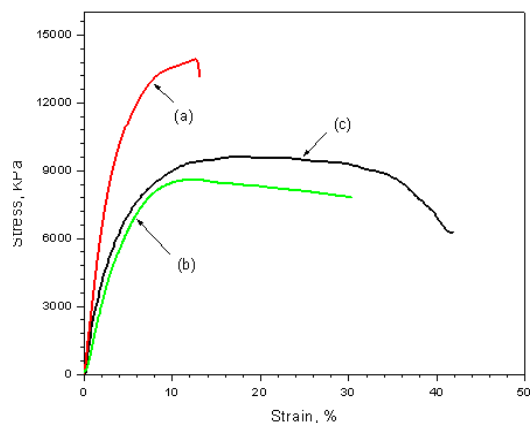

Fig 3: *Tensile stress-stain diagram: (a) sample at 0º orientation, (b) sample at 90º orientation and (c) neat polyethylene.*

4

observed that the melting temperatures as measured from the endothermic peaks are 129°C and 124°C for neat polyethylene and CNT-polyethylene, respectively. The results obtained from X-ray diffraction about crystallinity are therefore, consistent with these DSC tests; all indicating to the fact that nanocomposite is more crystalline than the neat polyethylene. Tension test results (Fig 3) reveal the fact that the ultimate failure stress of the 2% CNT reinforced polyethylene sample is about 34% higher than the neat sample. On the other hand, the improvement in tensile modulus due to CNT infusion is around 38%. Such gain in modulus is obviously a result of infusion of much stiffer material (CNTs) into a relatively softer material (LLDPE).

3.3 Nylon-6 reinforced with multi-walled carbon nanotubes (MWCNTs) [33]

Tensile tests of individual filaments were carried out to assess the increase in strength and stiffness of the nanophased nylon. Tests were performed in a regular MTS machine by taking machine compliance into account as per ASTM standard D3379-75. The Young's modulii of neat and nanophased filaments determined in this manner were found to be 1.1 GPa and 3.6 GPa, respectively.

Fig. 4 shows the stress-strain curves for samples of neat Nylon 6 and MWCNT-Nylon with 102 mm gage lengths. The 2% offset yield strength of the neat Nylon 6 was 35 MPa. The ultimate tensile strength was 125 MPa, and the strain to failure varied from 300% for the longest samples (102 mm gage length) to 800% for the shortest samples (13 mm gage length). With the limited displacement travel of the testing system, it was not possible to fail samples with 203 mm gage lengths.

The 2% offset yield strength of Nylon 6 with 1 wt% MWCNTs was 95 MPa. The ultimate tensile strength and strain to failure ranged from 330 MPa at 19% strain for the longest samples (102 mm gage length) to 410 MPa at 48% strain for the shortest samples (13 mm gage length). Presumably the trend of increasing ultimate tensile strength with decreasing gage length exhibited by both materials is due to a statistical distribution of flaws. The probability of sampling a flaw of sufficient size to precipitate failure increases with gage length, thereby decreasing the ultimate tensile strength and strain to failure. Note that for an addition of only 1 wt% MWCNTs, the strength of the composite material is more than twice that of the unreinforced Nylon which indicates the exceptional load-bearing capability of CNTs and their potential as structural materials. Such improvements were possible due to the alignment of nanotubes as shown in Fig.5.
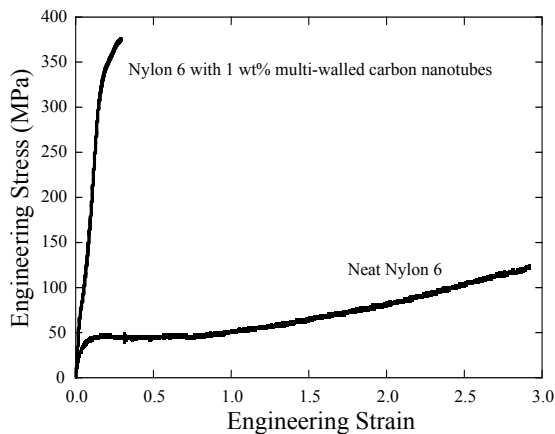

Fig 4: *Engineering stress versus engineering strain for neat Nylon, and Nylon with 1 wt% multi-walled carbon nanotubes with 102 mm gage lengths.*
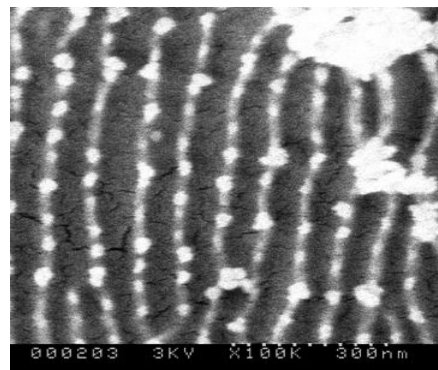

Fig 5: *FE-SEM micrograph showing alignment of MWCNTs in a nanophased filament. Filaments were milled with plasma in the presence of either argon or oxygen*

5

3.4 Nylon-6 infused with SiO₂ nanoparticles [34]

DSC heating test results indicate a moderate increase in the glass transition temperature and crystallinity, but reduction in the melting temperature of the nanophased material. From the area calculation and from the enthalpy of fusion the calculated degree of crystallinity was 24% and 27% for neat and the nanophased system, respectively. It is observed that the gain in failure strength and Young's modulus is around 36% and 28%, respectively. Dispersion of nanoparticles in the nanophased filament is shown in Fig 6, taken through a FE-SEM. SiO₂ nanoparticles are seen to be dispersed uniformly over the entire body of the matrix, and are coated with the polymer. Most of the coated particles are in the 20-40 nm range and there is no sign of agglomerations. Large white lumps seen in the figure are nylon which could not be removed by plasma etching.
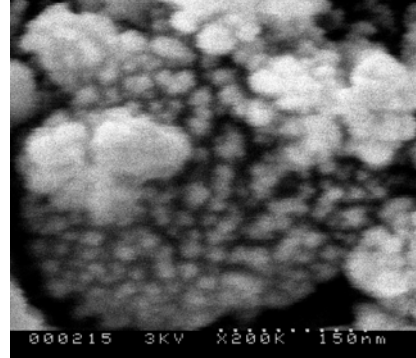

Fig 6: *Dispersion of SiO₂ nanoparticles in nanophased nylon*

3.5 Functionalized Silica nanoparticle reinforced Nylon -6 filament [35]

Organosilanes was used to modify the surface of silica nanoparticles. The inorganic compatibility comes from the alkoxy groups attached to the silicon atom. This bond is hydrolytically unstable and in the presence of moisture hydrolyses to an intermediate Si-OH bond which then condenses with surface bound OH groups on inorganic surfaces to form stable Si-O-Si bonds. When silica particles are silated (functionalized), the enhancement in strength and modulus increases by 76% and 55%, respectively as shown in Fig 7. It is also noticed that there is a loss of ultimate strain but it is still around 30% which is considerably high. Enhancement in stiffness and strength can be visualized from various aspects. Crystallinity of nylon 6 as determined by DSC was around 24%. With the addition of functionalized silica particles crystallinity increased to 29%. We have also noticed a corresponding shift in the crystalline temperature from 189^0C to 196^0C. The increase in stiffness is no doubt contributed by the higher stiffness (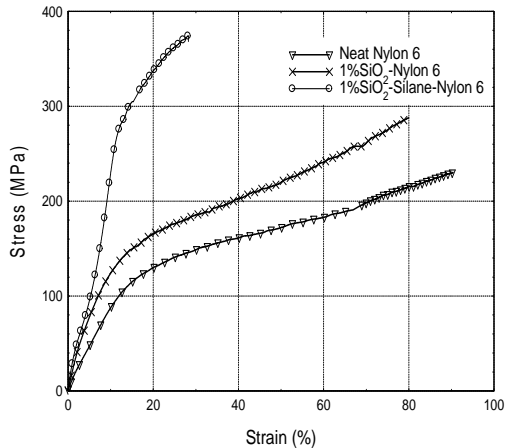nylon 1.1 GPa, silica 72.3 GPa) of the silica reinforcement. One order higher stiffness of silica would surely influence the stiffness of the composites simply from the rule of mixture concept. FTIR Spectroscopy curves are shown in Fig 8; a) neat nylon, b) nylon with 1 wt% SiO₂, and c) nylon with 1 wt% functionalized (silated) SiO₂. Three basic bonds of nylon 6, i.e., amide N-H @ 3297 cm^{-1}, hydroxyl O-H @ 2800-3000 cm^{-1}, and carbonyl C=O @ 1637 cm^{-1} were of primary interests. It is seen in Fig 8.b that IR absorbance for each of the three basic bonds has increased significantly characterized by their sharper and higher peaks. The IR absorbance is a direct measure of bond strength indicating that SiO₂ reinforcement into nylon was responsible for such increase. On the other hand after functionalization of SiO₂ particles, i.e., in

Fig 7*: Tensile tests of single filaments*

6

Fig 8.c it is seen that three basic bond strengths are maintained, while in addition, a siloxane Si-O-Si bond @1090 cm^{-1} is formed which was not seen with Fig 8.a or 8.b.This is what we expected from functionalization; establishing a continuous covalent linkage across the particle (silica) and polymer (Nylon 6) interface.
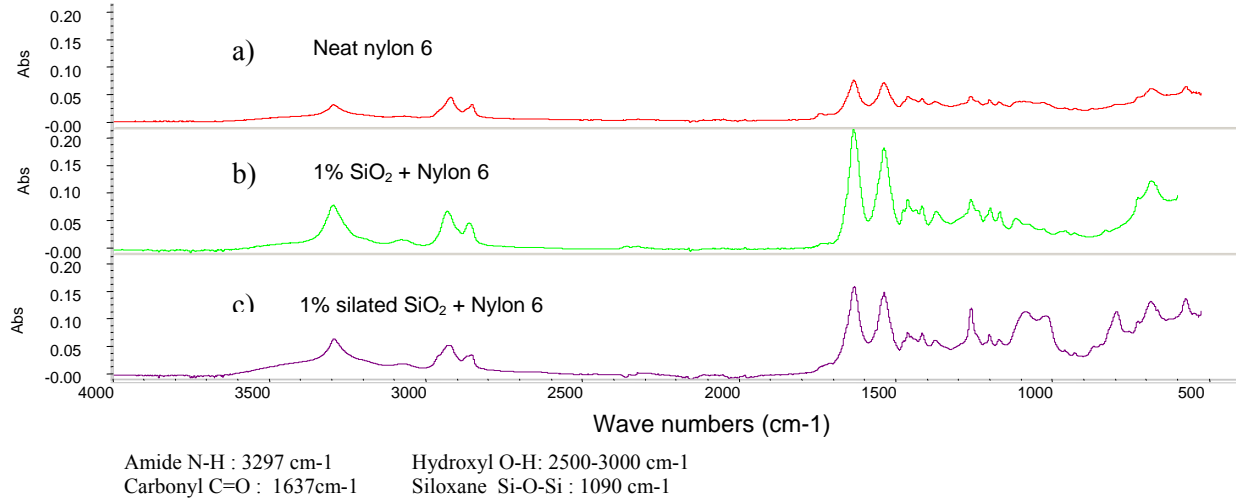

Amide N-H : 3297 cm-1   Hydroxyl O-H: 2500-3000 cm-1
Carbonyl C=O : 1637cm-1   Siloxane Si-O-Si : 1090 cm-1

Fig 8: *FTIR Spectroscopy – (a) neat nylon 6, (b) nylon 6 with 1wt% silica, and (c) nylon 6 with 1 wt% functionalized silica.*

3.6 LDPE reinforced with CNTs and UHMWPE [36]

XRD diffraction patterns of neat LDPE, LDPE–UHMWPE and LDPE–UHMWPE -CNT indicate that the samples have both crystallized and amorphous portions The Full-width at half maximum (FWHM) of 110 reflection were measured. Crystalline size was estimated from the equation, $D = K\lambda /\beta cos(\theta)$. Where D is the crystal size which is the thickness of the crystal perpendicular to the planes diffracting at Bragg angle θ, β is the FWHM for the peak in radian, λ and θ are the wavelength of X-ray and the diffraction angle respectively. K is a constant. In general, K depends on how to obtain the value of β. The value of K has been used as 0.9 because FWHM was obtained from XRD peak intensity [37]. The FWHM for the nanophased sample is found slightly less then the neat
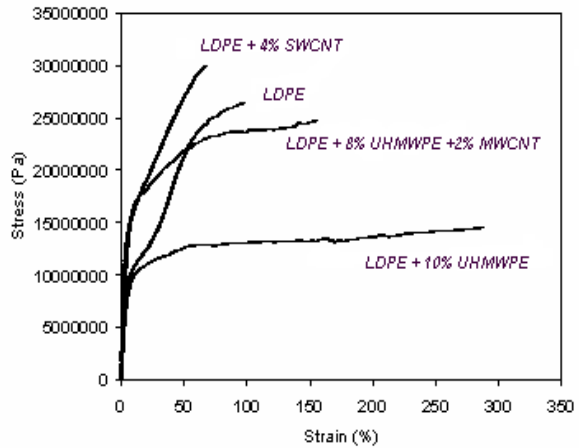
Fig 9: *Tensile stress-strain diagram*

Table 1

Sample	FWHM (Degree)	Crystalline size (Å)
Neat LDPE	0.51	158.7
LDPE with 10% UHMWPE	0.471	171.8
LDPE with 8% UHMWPE and 2% MWCNT	0.472	171.5
LDPE with 4% SWCNT	0.424	191.67

7

sample. But the difference was not that prominent. However the crystallite size was found to be higher in nanophased samples as shown in Table 1. From the DSC ramp test it is observed that the melting endotherm is wider in nanophased sample compared to the neat sample. There is a moderate increase in crystallinity with a reduction in melting temperature in the nanophased material. A representative stress-strain diagram from the filament tests is shown in Fig 9. It is observed from the filament tests that the fracture strain of LDPE has increased by about 200% with the addition of 10 wt% UHMWPE. This is however, is accompanied by a loss of about 50% ultimate tensile strength and 18% modulus. When 2 wt% MWCNTs and 8 wt% UHMWPE are added, tensile strength of the composite filament is restored to the level of neat LDPE (~ 25 MPa) with an increase in modulus by 44% and ultimate fracture strain by about 60% compared to that of neat LDPE. When only 4% SWCNT were infused in LDPE the strength and modulus increased by 5% and 52% respectively with a loss of fracture strain by about 35 %. It is reported that if LDPE is blended with UHMWPE an asymmetric polymer interface grows. Mechanical deformation theory also indicates that the high-volume fraction of polymer interfacial regions compared to that of the bulk materials leads to increased deformation by grain-boundary sliding and thus, increases fracture strain.

4. SUMMARY

A methodology using hot extrusion has been introduced to manufacture carbon nanoparticles/whiskers reinforced polyethylene filaments. Thermo Gravimetric Analysis (TGA) has indicated that nanoparticles/whiskers infusion increases the thermal stability and crystallinity of the system, which eventually translate into higher mechanical properties. The extrusion process has been extended to produce MWCNT infused nylon filaments which is vastly different from what is described elsewhere in the literature in a variety of ways, including melt extrusion and thermal stabilization procedures. The ultimate effect was in the spectacular enhancement (~200-300%) of mechanical properties of the nanophased nylon filaments. The source of this improvement is attributed to the successful alignment of nanotubes and the development of interfacial shear strength during the fabrication process.

It is also demonstrated that infusion of pristine silica nanoparticles can modestly increase the strength and modulus of nylon without any loss of fracture strain. FTIR analysis has shown that mere presence of silica nanoparticles can significantly influence the three primary bonds of nylon 6 resulting into 28% and 36% increase in modulus and strength, respectively. Once silica particles are functionalized, the enhancement in primary bonds are still retained, but a new silane bond is formed which improves the modulus and strength even further; by 55% and 76%, respectively. The source of the improvement is traced to: (i) increase in the concentration of basic bonds nucleated by the presence of nanoparticles, (ii) formation of siloxane bond, and (iii) changes in the fracture process induced by the infused silica particles. Fracture studies of filaments have revealed that after functionalization nylon 6 seems to exhibit brittle failure modes, but still retains high strength with 30% ultimate strain.

It is shown that with the infusion of UHMWPE, ultimate fracture strain of the composite can be increased by about 200% when compared with neat LDPE. But this is accompanied by a significant loss in strength and modulus. When both MWCNTs and UHMWPE are infused with LDPE, the improvement in fracture strain is reduced to 60% while the modulus increases by 44%. Although there is no improvement in strength, it recovers to the level of neat LDPE. If functionalized SWCNTs and UHMWPE were both infused with LDPE, the extruded filament became extremely brittle.

8

REFERENCES

[1] Teishev A, Incardona S, Migliaresi C, Marom G, Polyethylene fibers-polyethylene matrix composites: preparation and physical properties, *Journal of Applied Polymer Science* 1993; 5: 503-512.

[2] Sperling L H, Introduction to Physical Polymer Science, 2nd edition, John Willey & Sons, Inc., New York, USA. 1992.

[3] Hlangothi S P, Krupa I, Djokovic V, Luyt A S, Thermal and mechanical properties of cross-linked and uncross-linked linear low-density polyethylene–wax blends*, Polymer Degradation and Stability* 2003; 79: 53-59.

[4] Walter R, Friedrich K, Privalko V, Savadori A. On Modulus and fracture toughness of rigid particulate filled high density polyethylene, *Journal of Adhesion* 1997; 64: 87-109.

[5] Rothan R N, Mineral fillers in thermoplastics: filler manufacture and characterization, *Advanced Polymer Science* 1999; 139: 67-107.

[6] Wu C L, Zhang M Q, Rong M Z, Friedrich K, Tensile performance improvement of low nanoparticles filled-polypropylene composites, *Composite Science and Technology* 2002; 62: 1-13.

[7] Kuriger R J, Alam M K, Anderson D P, Jacobsen R L, Processing and characterization of aligned vapor grown fiber reinforced polypropylene, *Composites: Part A*, 2002; 33: 53-62.

[8] Tibetts G G, Macugh J J, Mechanical Properties of vapor grown carbon fiber composites with thermoplastic matrices, *Journal of Material Research* 1999; 14(7): 2871-2880.

[9] Sandler J, Werner P, Shaffer M S P, Demchuk V, Alstadt V, WIndle A H, Carbon-naofibre-reinforced poly(ether ether ketone) composites, *Composites: Part A*, 2002; 33-1039.

[10] Jung S W, Kim S Y, Nam H W, Han K S, Measurements of fiber orientation and elastic-modulus analysis in short-fiber-reinforced composites, *Composites Science and Technology*, 2001; 7-116.

[11] Cooper C A, Ravich D, lips D, Mayer J, Wagner H D, Distribution and alignment of carbon nanotubes and naofibrils in a polymeric matrix, *Composites Science and Technology*, 2002; 62: 1105-1112.

[12] Jarrin J, Vinciguerra E, Ausias G, Vincent M, Dawans F, Extrusion of tubes of fiber-reinforced thermoplastics, U.S. Patent No. 1994; 5: 307: 843.

[13] Wang Y, Huang J S, Single screw extrusion compounding of particulate filled thermoplastics: state of dispersion and its influence on impact properties*, Journal of Applied Polymer Science* 1996; 60: 1779-1791.

[14] Cho J W, Paul D R, Nylon 6 nanocomposites by melt compounding , *Polymer*, 2001; 42: 1083-1094.

[15] Dennis H R, Hunter D L, Chang D, Kim S, White J L, Cho J W, Paul D R, Effect of melt processing conditions on the extent of exfoliation in organoclay-based nanocomposites 2001; 42: 9513-9522.

[16] Salvent J. P., Briggs G. A. D., Bonard J. M., Bacsa R. R., Kulik A. J., Stockli T., Burnham N. A., Forro L., *Physical Review Letters*, 82(5), 944-947, 1999.

[17] Li F., Cheng H. M., Bai S., Su G., Dresselhaus M. S., *Applied Physics Letters*, 77(20), 3161-3163, 2000.

[18] Li C, Chou TW, *Composite Science and Technology*, 63, 1517-1524, 2003.

[19] Jin L, Bower C, Zhou O, *Applied Physics Letter*,73, 1197-1199, 1998.

[20] Cooper C. A., Ravich D., lips D., Mayer J., Wagner H. D., *Composites Science and Technology*, 62, 1105-1112, 2002.

[21] Thostenson ET, Chou TW, *Journal of Physics D: Applied Physics*, 35(16), L77-80, 2002.

[22] Kohan M. I, editor. Nylon Plastics, John Wiley & Sons, New York 1973, p.3-4.

9

[23] Fornes TD, Paul D.R., *Polymer*, 44, 3945, ., 2003

[24] Kim, Young, Materials Research Society Symposium - Proceedings, 2002, V740, 441

[25] Zhang, Wei-De, *Macromolecular Rapid Communications*, 2004,V 25, n 21, 1860.

[26] Jin L, Bower C, Zhou O. *Appl Phys*, 1998 Lett, 73, 1197.

[27] S. M. Kurtz, O. K. Muratogiu, M. Evans, A. A. Edidin, Advances in the processing, sterilization, and crosslinking of ultra-high molecular weight polyethylene for total joint arthoplasty, *Biomaterials*, 20:1659 -1688, (1999)

[28]A. Bellare, H. Schanblegger, and R. E. Cohen. A small angel X-ray scattering study of high density polyethylene and ultra-high molecular weight polyethylene, *Macromolecules,* 17:2325- 2333, (1995)

[29] Mahfuz H, Adnan A, Rangari V. K, Jeelani S, Carbon Nanoparticles/ Whiskers Reinforced Composites and their Tensile Response, *Composites Part A:Applied Science and Manufacturing*, 2004, Vol. 35, pp.519-527

[30] Mahfuz H, Adnan A, Rangari V. K, Jeelani S, Manufacturing and characterization of carbon nanotube / polyethylene composites, *International Journal of Nanoscience*, 2005, Vol 4, No. 1, pp. 55-72.

[31] Kevin P, Ryan, Stephen M, Lipson, Drury A, Cadek M, Ruether M, O'Flaherty S. M, Barron V, McCarthy B, Byrne H. J, Werner J, Blau and Coleman J. N, Carbon-nanotube nucleated crystallinity in a conjugated polymer based composites, *Chemical Physics Letters*, 2004,391, pp. 329 -333.

[32] Taniguchi A and Cakmak M, The suppression of strain induced crystallization in PET through submicron TiO_2 particle incorporation, *Polymer*, 2004, 45, pp. 6647–6654

[33] Mahfuz H, Adnan A, Rangari V. K, Jeelan S, Hassan M. M, Wright W. J, Deteresa S. J, Enhancement of strength and stiffness of nylon 6 filaments through carbon nanotubes reinforcement, *Appl Phys Lett*, 2006, 88, 083119

[34] Mahfuz H,. Hassan M. M,. Rangari V. K, Jeelani S, Reinforcement of nylon 6 filaments with SiO_2 nanoparticles and comparison of young's modulus with theoretical bounds, *Macromol. Mater. Eng.*2007, 292, pp. 437-444

[35] Mahfuz H, Hassan M. M, Dhanak V, Beamson G, Stewart J, Rangari V, Wei X, Khabashesku V, and Jeelani S, Reinforcement of nylon 6 with functionalized silica nanoparticles for enhanced tensile strength and modulus, *Nanotechnology*, 2008, 19, 445702, pp.7

[36] Khan M. R, Mahfuz H. and Leventouri T, Investigation of infusion of ultra high molecular weight polyethylene (UHMWPE) and carbon nanotube (CNT) into low density polyethylene (LDPE) filaments, *SAMPE Fall technical conference*, Sept. 8-11,2008, Memphis, Tennesse

[37] Bunn C. W, Chemical crystallography an introduction to optical and X-Ray methods, Oxford University Press, 1961.